Topographically Generated Submesoscale Shear Instabilities Associated with Brazil Current Meanders

CAIQUE D. LUKO[®], a CAUÊ Z. LAZANEO, ILSON C. A. DA SILVEIRA, FILIPE PEREIRA, A. DA MIT TANDON^{b,c}

^a Instituto Oceanográfico, Universidade de São Paulo, São Paulo, Brazil
^b School for Marine Science and Technology, University of Massachusetts Dartmouth, New Bedford, Massachusetts
^c Mechanical Engineering Department, University of Massachusetts Dartmouth, Dartmouth, Massachusetts

(Manuscript received 3 June 2022, in final form 24 March 2023, accepted 29 March 2023)

ABSTRACT: The western boundary current system off southeastern Brazil is composed of the poleward-flowing Brazil Current (BC) in the upper 300 m and the equatorward flowing Intermediate Western Boundary Current (IWBC) underneath it, forming a first-baroclinic mode structure in the mean. Between 22° and 23°S, the BC-IWBC jet develops recurrent cyclonic meanders that grow quasi-stationarily via baroclinic instability, though their triggering mechanisms are not yet well understood. Our study, thus, aims to propose a mechanism that could initiate the formation of these mesoscale eddies by adding the submesoscale component to the hydrodynamic scenario. To address this, we perform a regional 1/50° (~2 km) resolution numerical simulation using CROCO (Coastal and Regional Ocean Community model). Our results indicate that incoming anticyclones reach the slope upstream of separation regions and generate barotropic instability that can trigger the meanders' formation. Subsequently, this process generates submesoscale cyclones that contribute, along with baroclinic instability, to the meanders' growth, resulting in a submesoscale-to-mesoscale inverse cascade. Last, as the mesoscale cyclones grow, they interact with the slope, generating inertially and symmetrically unstable anticyclonic submesoscale vortices and filaments.

SIGNIFICANCE STATEMENT: Off southeastern Brazil, the Brazil Current develops recurrent cyclonic meanders. Such meanders enhance the open-ocean primary productivity and are of societal importance as they are located in a region rich in oil and gas where oil-spill accidents have already happened. This study aims to explore the processes responsible for triggering the formation of these mesoscale eddies. We find that incoming anticyclones reach the slope upstream of separation regions and generate barotropic instabilities that eject submesoscale filaments and vortices and can trigger the meanders' formation. Such results show that topographically generated submesoscale instabilities can play an important role in the dynamics of mesoscale meanders off southeastern Brazil. Moreover, this may indicate that resolving the submesoscale dynamics in operational numerical models may contribute to an increase in the predictability of the regional eddies.

KEYWORDS: Boundary currents; Instability; South Atlantic Ocean

1. Introduction

a. Topographically generated submesoscale motions

Submesoscale phenomena are dynamically distinguished by their Rossby (Ro = ζ/f) and Richardson (Ri = $N^2/|\partial \mathbf{v}/\partial z|^2$) numbers of $\mathcal{O}(1)$ (Thomas et al. 2008; McWilliams 2016; Gula et al. 2022; Taylor and Thompson 2023), where ζ is the relative vorticity, f is the planetary vorticity, N^2 is the stratification, and \mathbf{v} is the velocity vector. Such phenomena occur in the transition between the two-dimensional quasigeostrophic mesoscale and the isotropic small scale, assuming horizontal scales of 100 m to 10 km and time scales of hours to weeks (Thomas et al. 2008; McWilliams 2016). For a long time, the investigation of submesoscale motions encountered an operational barrier due to their spatiotemporal scales. However,

Luko's current affiliation: Scripps Institution of Oceanography, University of California, San Diego, La Jolla, California.

Corresponding author: Caique D. Luko, cdiasluko@ucsd.edu

increased spatial resolution in both observations and modeling has shown the abundance of submesoscale processes as well as their importance: (i) to cascade energy from the mesoscale to energy dissipation scales (e.g., Müller et al. 2005); (ii) to restratify the upper ocean (e.g., Fox-Kemper et al. 2008); and (iii) to the vertical exchange of tracers and, consequently, to structure marine ecosystems (e.g., Mahadevan 2016; Lévy et al. 2018; Fadeev et al. 2021; Freilich and Mahadevan 2021).

Submesoscale motions can arise through mixed layer baroclinic instabilities, mesoscale strain leading to frontogenesis, atmospheric destabilizing forcing, and flow interactions with topography (Gula et al. 2022). In particular, submesoscale motions generated by flow–topography interactions can play a key role in the generation of mesoscale meanders downstream of separation regions. Off the U.S. East Coast, for instance, the Gulf Stream crosses the Charleston Bump and generates barotropic instabilities (Gula et al. 2016a). During this process, submesoscale cyclones are ejected offshore, and subsequently, mesoscale meanders grow downstream. By contrast, off the U.S. West Coast, the California Undercurrent generates inertial instabilities while crossing separation regions

(Molemaker et al. 2015). Subsequently, submesoscale anticyclones are ejected offshore and contribute to the growth of mesoscale anticyclones in a submesoscale-to-mesoscale inverse cascade.

Submesoscale motions can trigger the formation of mesoscale meanders, but the opposite is also true. The interaction of mesoscale meanders with topography can ignite symmetric and inertial instabilities (Napolitano et al. 2021a), and generate submesoscale coherent vortices (SCVs) (Lazaneo et al. 2022). Such processes can enhance the vertical exchange of tracers and lead to energy dissipation (Gula et al. 2016b; Lazaneo et al. 2022).

Off southeastern Brazil, Brazil Current (BC) mesoscale cyclones are generated downstream of separation regions, and grow quasi-stationarily adjacent to the shelf break (da Silveira et al. 2008). Thus, submesoscale flow-topography processes might be important to both (i) the generation of BC meanders and (ii) the development of symmetric/inertial instabilities, and subsequent formation of SCVs.

b. The Brazil Current and its meanders

The BC is the western boundary current that closes the South Atlantic subtropical gyre (Stramma and England 1999). The BC arises at the surface South Equatorial Current branch bifurcation at about 14°S as a mixed layer poleward jet that transports Tropical Water (Rodrigues et al. 2007; Soutelino et al. 2011; Luko et al. 2021). It increases its vertical extension and transport as it receives the inflow of South Atlantic Central Water (SACW) and Antarctic Intermediate Water (AAIW) coming from different impinging South Equatorial Current bands (Soutelino et al. 2011; Luko et al. 2021). For instance, at about 23°S, the BC occupies the upper $\sim\!350$ m and transports 1–5 Sv (1 Sv \equiv 10^6 m³ s $^{-1}$), while south of 27°S it spans the upper $\sim\!800$ m and transports 10–20 Sv (Rocha et al. 2014; Schmid and Majumder 2018).

Off southeastern Brazil, the western boundary current system is formed by the BC, which occupies the upper 200–350 m, and the underlying equatorward-flowing Intermediate Western Boundary Current (IWBC), which spans from ~200–350 to ~1800 m (da Silveira et al. 2004; Napolitano et al. 2019). With this configuration, the BC-IWBC jet dissipates energy due to intense vertical shear (Lazaneo et al. 2020), and develops recurrent mesoscale meanders through baroclinic instability (da Silveira et al. 2008; Rocha et al. 2014; da Silveira et al. 2023). These meanders are known to play a relevant role in coastal upwelling (Calado et al. 2010; Palóczy et al. 2014), in transporting shelf waters to the open ocean (Mill et al. 2015), and in modulating the regional biogeochemical dynamics (Pereira et al. 2019).

The BC is prone to baroclinic instability from 20° to 36°S (Magalhães et al. 2017). In particular, recurrent mesoscale activity is observed off southeastern Brazil (Rocha and SimoesSousa 2022; Uchoa et al. 2023; da Silveira et al. 2023) as the BC crosses two separation regions: (i) Cape São Tomé (CST, ~22°S) and (ii) Cape Frio (CF, ~23°S). As the BC passes the capes, barotropic instabilities happen upstream, while

baroclinic instabilities happen downstream (Magalhães et al. 2017).

As seen in section 1a, topographically generated submesoscale shear instabilities can contribute to the formation and growth of mesoscale meanders. To our knowledge, there are no studies that investigate the role of submesoscale motions on the BC meander dynamics. Consequently, there is also no information on how the submesoscale relates to the barotropic and baroclinic instabilities observed in mesoscale studies.

In this work, we aim to answer whether or not (i) submeso-scale shear instabilities generated by flow-topography interactions can play a role in the formation of BC meanders between 22° and 23°S, (ii) submesoscale features contribute to the growth of the BC meanders in a submesoscale-to-mesoscale inverse cascade, and (iii) the interaction of the BC cyclones with topography generates submesoscale instabilities and submeso-scale vortices.

We organize this work as follows. In section 2 we describe our numerical setup and the methods to diagnose submesoscale instabilities and perform the energy analyses. In section 3 we show and discuss our results and in section 4 we summarize our results and draw our conclusions.

2. Methods

a. Numerical simulation

We perform a high-resolution numerical simulation using CROCO (Coastal Regional Oceanic Community model) in the hydrostatic mode. CROCO is built upon ROMS-AGRIF (Regional Ocean Model System–Adaptative Mesh Refinement in Fortran) and solves the free surface, hydrostatic, and primitive equations in terrain-following coordinates using a time-splitting implementation (Shchepetkin and McWilliams 2005). We run the model between 50° – 30° W and 28° – 17° S (Fig. 1) and use a horizontal resolution of $1/50^{\circ}$ (\sim 2 km) with 30 sigma levels. The sigma level stretching parameters are set to achieve higher resolutions near the surface and the bottom ($\theta_s = 6$, $\theta_b = 4$, and $h_c = 50$).

The initial and boundary conditions are obtained from the 1/12° GLORYS12V1 daily reanalysis (Fernandez and Lellouche 2018). The model is forced by 6-hourly ERA5 atmospheric bulk fluxes (Hersbach et al. 2020) and TPX07 tides (Egbert and Erofeeva 2002). The bathymetry is extracted from the General Bathymetric Chart of the Oceans (GEBCO) 2021 and filtered to limit the maximum $\nabla h/h$ to 0.25 in order to prevent horizontal pressure gradients errors that are common in terrain-following coordinate models (Haney 1991). The simulation spans from 2015 to 2019 and has one year of spinup. Although the simulation is dated, we do not intend to reproduce specific events. Rather, we aim to simulate realistic events that capture the submesoscale dynamics associated with the BC meanders (see appendix for details on the model evaluation). In particular, we analyze two CST cyclone events: one in the spring of 2016, and the other in the transition between summer and fall of 2019.

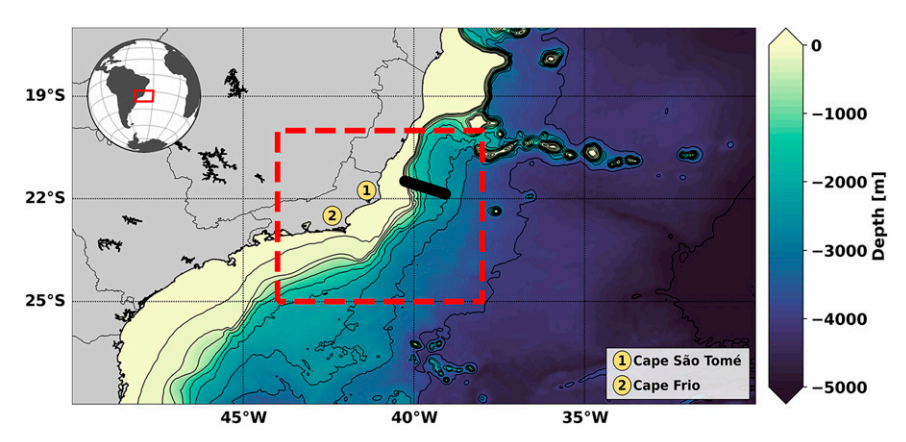


FIG. 1. Model domain and filtered GEBCO2021 topography. The red dashed box and the black transect are areas used for the model evaluation (see the appendix).

We use a fifth-order upwind scheme for the horizontal advection and fourth-order centered schemes for the vertical advection of momentum and tracers. Both high-order schemes are of higher accuracy and reduce spurious diapycnal mixing (Soufflet et al. 2016). We include vertical mixing in the simulation using the K-profile parameterization (KPP). On the other hand, numerical constraints control horizontal mixing as we solve the horizontal advection with an upwind scheme. For the fifth-order scheme, dissipation extends to wavelengths of $5\Delta x$ (submesoscale vortices with 5-km diameters). Last, bottom friction is parameterized in the model using a linear function with a drag coefficient of $3 \times 10^{-4} \, \mathrm{m \, s^{-1}}$.

b. Potential vorticity analysis

Assuming that $2\Omega = f\mathbf{k}$, the Ertel potential vorticity (q) is equal to

$$q = \boldsymbol{\omega}_{a} \cdot \nabla b = \underbrace{(f + \zeta)N^{2}}_{q_{\text{vert}}} + \underbrace{\left(\frac{\partial u}{\partial z} - \frac{\partial w}{\partial x}\right)\frac{\partial b}{\partial y} + \left(\frac{\partial w}{\partial y} - \frac{\partial v}{\partial z}\right)\frac{\partial b}{\partial x}}_{q_{\text{bc}}},$$

$$\tag{1}$$

where ω_a is the absolute vorticity; b is the buoyancy $(-g\rho/\overline{\rho})$; g is the acceleration due to gravity; ρ is the density; u, v, and w are the zonal, meridional, and vertical velocity components, respectively; q_{vert} is the vertical component of q; and q_{bc} is the baroclinic component of q.

A consequence of the Ertel potential vorticity theorem [Eq.(1)] is that, in a baroclinic fluid, conservation of q implies conservation of buoyancy (e.g., Buckingham et al. 2021a). In the interior ocean, q is approximately conserved and the product fq is always positive. However, close to the boundaries where diabatic processes can occur due to the intensification of friction and buoyancy fluxes, q can be injected/extracted.

Injection of q in the bottom boundary layer (BBL) occurs when the shear between flow and topography increases cyclonic vorticity. On some occasions, q injection can lead to barotropic instability (e.g., Gula et al. 2015, 2016a). Here, we

use q along with Ro to find events where the BC might be developing barotropic shear instability.

Extraction of q in the BBL, on the other hand, occurs when the shear between flow and topography increases anticyclonic vorticity. During this process, the product fq can become negative and submesoscale instabilities can be developed in thermal-wind-balanced fronts (Thomas et al. 2013). If fq becomes negative due to $N^2 < 0$, the instability is a barotropic flow, inertial instability occurs. Last, if fq < 0 with $fq_{\rm vert} < 0$ and $fq_{\rm vert} > 0$, symmetric instability occurs. In addition, different combinations of the fq components can lead to mixed instability regimes. Based on energy exchange rates for a thermal-wind-balanced flow, Thomas et al. (2013) have shown that these different instability regimes can be differentiated by the following angles:

$$\phi_{\text{tw}} = \tan^{-1} \left(-\frac{1}{\text{Ri}_B} \right) = \tan^{-1} \left(-\frac{|\nabla_h b|^2}{f^2 N^2} \right),$$
 (2)

$$\phi_{\text{tw}_c} = \tan^{-1} \left(\frac{\zeta_g}{f} \right), \tag{3}$$

where Ri_B is the bulk Richardson number $(=f^2N^2/|\nabla_h b|^2)$, ζ_g is the geostrophic relative vorticity, ϕ_{tw} is the thermal-wind Thomas angle, and ϕ_{tw_c} is the thermal-wind critical angle. See the instability categories according to these angles in Table 1.

Although very useful, the fq < 0 criterion does not yield a generalized sufficient criterion for submesoscale instabilities. The sufficient criterion arises when centrifugal effects are taken into account (gradient-wind balanced flows). Buckingham et al. (2021a,b) have shown that the product between Ertel's potential vorticity and absolute angular momentum must be positive in an inviscid front for stability. Instability occurs if

$$(1 + Cu)fq < 0, (4)$$

where the curvature number $Cu = 2V_g/(fr)$, V_g is the geostrophic speed (e.g., Balwada et al. 2021), and r the local

TABLE 1. Instability categories for thermal-wind balanced flows (TWB) according to ϕ_{tw} and ϕ_{tw} (Thomas et al. 2013), and instability categories for gradient-wind balanced flows (GWB) according to ϕ_{gw} and ϕ_{gw} (Buckingham et al. 2021a). Categories: stable (St.), symmetric (S), inertial (I), and gravitational (G).

Instability	Thomas angle			
	TWB		GWB	
	Cyclonic	Anticyclonic	Cyclonic	Anticyclonic
St.	$\phi_{\mathrm{tw}_c} < \phi_{\mathrm{tw}} \le 0$	$\phi_{\mathrm{tw}_c} < \phi_{\mathrm{tw}} \le 0$	$\phi_{\mathrm{gw}_c} < \phi_{\mathrm{gw}} \le 0$	$\phi_{\mathrm{gw}_c} < \phi_{\mathrm{gw}} \le 0$
S + I	_	$-rac{\pi}{4}$ $<$ ϕ_{tw} \le ϕ_{tw_c}	_	$-\frac{\pi}{4} < \phi_{\mathrm{gw}} \le \phi_{\mathrm{gw}_c}$
S	$-\frac{\pi}{2} < \phi_{\mathrm{tw}} \le \phi_{\mathrm{tw}_c}$	$-\frac{\pi}{2} < \phi_{\rm tw} \le -\frac{\pi}{4}$	$-\frac{\pi}{2} < \phi_{\mathrm{gw}} \le \phi_{\mathrm{gw}_c}$	$-\frac{\pi}{2} < \phi_{\rm gw} \le -\frac{\pi}{4}$
G + S	$-\frac{3\pi}{4} < \phi_{\rm tw} \le -\frac{\pi}{2}$	$-\frac{3\pi}{4} < \phi_{\rm tw} \le -\frac{\pi}{2}$	$-\frac{3\pi}{4} < \phi_{\rm gw} \le -\frac{\pi}{2}$	$-\frac{3\pi}{4} < \phi_{\rm gw} \le -\frac{\pi}{2}$
G	$-\pi < \phi_{\rm tw} \le -\frac{3\pi}{4}$	$-\pi < \phi_{\rm tw} \le -\frac{3\pi}{4}$	$-\pi < \phi_{\rm gw} \le -\frac{3\pi}{4}$	$-\pi < \phi_{\rm gw} \le -\frac{3\pi}{4}$

radius of curvature (Theisel and Rauschenbach 1999; Balwada et al. 2021):

$$r = \frac{(u_g^2 + v_g^2)^{3/2}}{u_g^2 \frac{\partial v}{\partial x} - v_g^2 \frac{\partial u}{\partial y} + u_g v_g \left(\frac{\partial v}{\partial y} - \frac{\partial u}{\partial x}\right)},$$
 (5)

where u_g and v_g are the zonal and meridional geostrophic velocities, respectively. In this study, we consider nondivergent velocities to be approximately geostrophic, and use them to compute r and Cu. These nondivergent velocities are obtained by applying the algorithm from Li et al. (2006).

Equation (4) is the generalized Rayleigh criterion (Buckingham et al. 2021a). This criterion shows that an exchange of vorticity, stratification, and centripetal accelerations must happen so that stability can be attained. Note that it reduces to the criterion originally used for thermal-wind-balanced fronts (fq < 0) when centrifugal effects are negligible [$\lim_{r\to\infty} Cu(r) = 0$].

Based on the nondimensional product of the Ertel potential vorticity and the absolute angular momentum, Buckingham et al. (2021a) modified the instability angles introduced by Thomas et al. (2013):

$$\phi_{\text{tw}} \to \phi_{\text{gw}} = \tan^{-1} \left[-\frac{(1 + \text{Cu})^2}{\text{Ri}} \right],$$
 (6)

$$\phi_{\text{tw}_c} \to \phi_{\text{gw}_c} = \tan^{-1}[-(1 + \text{Cu})(1 + \text{Ro})],$$
 (7)

where $\phi_{\rm gw}$ is the gradient-wind Thomas angle, and $\phi_{\rm gw}_c$ is the gradient-wind critical angle. See the instability categories according to $\phi_{\rm gw}$ and $\phi_{\rm gw}$ in Table 1. This instability classification shows which aspect of the flow is the most responsible for reducing the $(1 + {\rm Cu})fq$ discriminant, but it should not be interpreted in terms of energy exchange under linear instability as the classification from Thomas et al. (2013). In this work, we use the generalized Rayleigh criterion and the gradient wind Thomas angle $(\phi_{\rm gw})$ to investigate the occurrence of symmetric and inertial instabilities associated with the BC meanders' interaction with the topography.

c. Energy conversions

As shown in section 2b, symmetric, inertial, and gravitational instabilities arise if the generalized Rayleigh discriminant becomes negative. However, some submesoscale instabilities, such as barotropic shear instability (e.g., Gula et al. 2015, 2016a), may occur even if the product (1 + Cu)fq is positive. Since the Thomas angle does not capture this positive (1 + Cu)fq instability, we analyze energy conversions to investigate the occurrence of barotropic shear instability. Baroclinic instability plays an important role in the dynamics of the BC meanders' growth off CST and CF (da Silveira et al. 2008; Rocha et al. 2014). We take advantage of the energy conversion analysis and also assess the occurrence of baroclinic instability during the growth of these meanders.

From the eddy kinetic energy (EKE) and the eddy potential energy (EPE) conservation equations (e.g., Chen et al. 2014; Magalhães et al. 2017; Napolitano et al. 2019; Li et al. 2022; Li and Roughan 2023) we analyze three terms: the horizontal shear production [HSP, Eq. (8)],

$$HSP = -\overline{u'^2} \frac{\partial \overline{u}}{\partial x} - \overline{u'v'} \frac{\partial \overline{u}}{\partial y} - \overline{v'^2} \frac{\partial \overline{v}}{\partial y} - \overline{u'v'} \frac{\partial \overline{v}}{\partial x};$$
(8)

the buoyancy production [BP, Eq. (9)],

$$\underline{\mathbf{BP} = -\left(\frac{1}{N^2}\right)\left(\overline{u'b'}\frac{\partial\overline{b}}{\partial x} + \overline{v'b'}\frac{\partial\overline{b}}{\partial y} + \overline{w'b'}\frac{\partial\overline{b}}{\partial z}\right)};$$
(9)

and the buoyancy flux [BF, Eq. (10)],

$$\underbrace{\text{BF} = \overline{w'b'}}_{\text{EPE} \to \text{EKE}} .$$
(10)

The overbars denote time averages, and the primes are the deviations from that average. We adopt 7-day means to investigate the occurrence of instabilities during the generation and growth of the mesoscale cyclones.

The HSP term shows the transfer of energy from the mean kinetic energy (MKE) to the EKE (Chen et al. 2014).

Negative HSP denotes the pathway EKE \rightarrow MKE while positive HSP denotes MKE \rightarrow EKE which occurs through horizontal shear instabilities. The BP term shows the transfer of energy from the mean potential energy (MPE) to the EPE, while the BF term shows transfers from EPE to EKE (Chen et al. 2014). Analogously to the HSP, negative BP (BF) means a EPE \rightarrow MPE (EKE \rightarrow EPE) transfer, while positive BP (BF) means a MPE \rightarrow EPE (EPE \rightarrow EKE) transfer. If BP and/or BF are positive, we have a signal of baroclinic instabilities (Kang and Curchitser 2015; Yan et al. 2019, 2022).

d. Kinetic energy flux across scales

Traditionally, kinetic energy (KE) fluxes are measured using spectral methods. However, these methods rely upon the assumption of statistical homogeneity or a large-scale separation between the eddying scales of motion and the scales over which the statistics vary (e.g., Aluie et al. 2018). By contrast, the so-called "coarse-graining" approach is capable of quantifying kinetic energy fluxes across scales in any geographic location and instant of time, without relying on assumptions of homogeneity or isotropy (e.g., Aluie et al. 2018; Schubert et al. 2020, 2021). Here, we use this method to quantify the kinetic energy fluxes between submesoscale motions and larger scale flows.

The method is applied as follows. For a scalar field, such as the zonal velocity component, we obtain a low-pass-filtered field by applying the convolution

$$\overline{u(x, y)} = C \times u(x, y), \tag{11}$$

where C is a normalized window function, and $\overline{u(x, y)}$ is a low-pass-filtered field which only contains scales larger than the length scale L. Following Aluie et al. (2018), we choose C to be the top-hat kernel:

$$C(\mathbf{R}) = \begin{cases} 1/A, & \text{if } |\mathbf{R}| < L/2\\ 0, & \text{otherwise,} \end{cases}$$
 (12)

where $A = \pi L^2/4$ is the normalization area with diameter L, and **R** is the radial position vector.

We apply this convolution to all the velocity components and obtain the low-passed-filtered fields $\overline{\mathbf{u}} = (\overline{u}, \overline{v}, \overline{w})$. The equations of motion do not change their form when we apply this convolution (Aluie et al. 2018). There is only one new term that arises from the nonlinear advection term:

$$\nabla \cdot \overline{\mathbf{u}\mathbf{u}} = \nabla \cdot \overline{\mathbf{u}} \, \overline{\mathbf{u}} + \nabla \cdot \overline{\tau}(\mathbf{u}, \, \mathbf{u}). \tag{13}$$

where $\overline{\tau}(\mathbf{u}, \mathbf{u}) = \overline{\mathbf{u}}\overline{\mathbf{u}} - \overline{\mathbf{u}}\overline{\mathbf{u}}$ is called the subfilter stress tensor that consists of the force that the unfiltered motions exert on the low-pass-filtered flow.

To obtain the kinetic energy flux expression, we need to compute the large-scale kinetic energy budget. This is done by multiplying the momentum equations by $\rho_0 \overline{\mathbf{u}}$. When multiplying the subfilter stress by $\rho_0 \overline{\mathbf{u}}$, we obtain:

$$\rho_0 \overline{\mathbf{u}} \cdot [\overline{\tau}(\mathbf{u}, \mathbf{u})] = \nabla \cdot [\rho_0 \overline{\mathbf{u}} \overline{\tau}(\mathbf{u}, \mathbf{u})] + \Pi. \tag{14}$$

The first term on the right-hand side is the divergence of the transport of large-scale kinetic energy by small-scale currents, while the second term is the kinetic energy flux across scales (Π):

$$\Pi = -\rho_0 \left\{ \left[\overline{u^2} - \overline{u}^2 \right] \frac{\overline{\partial u}}{\partial x} + \left[\overline{u}\overline{v} - \overline{u}\,\overline{v} \right] \left[\frac{\overline{\partial u}}{\partial y} + \frac{\overline{\partial v}}{\partial x} \right] + \left[\overline{v^2} - \overline{v}^2 \right] \frac{\overline{\partial v}}{\partial y} \right\}, \tag{15}$$

where negative (positive) values denote upscale (downscale) kinetic energy fluxes. Here, we compute Π to check if a submesoscale-to-mesoscale inverse cascade contributes to the growth of the BC mesoscale meanders as in the California Undercurrent case (Molemaker et al. 2015). As the first internal Rossby deformation radius (R_d) is ~25 km in the region (Houry et al. 1987), we adopt L=50 km as the transition scale between submesoscale and mesoscale flows.

Following Aluie et al. (2018), we impose velocities prior to the filtering process to be equal to zero on land. This is done to obtain results near the boundaries, as the convolution kernel needs to take information over a region with a diameter L. Consequently, there is some uncertainty on interpreting results that are over a distance of L/2 from the boundary (25 km in our case).

Last, although our grid is not truly regular, the difference between Δx and Δy extremes is of about 60 m inside the domain ($\sim 10^2$ smaller than the horizontal resolution of ~ 2 km). Hence, we consider our grid approximately Cartesian in physical space and compute the fluxes using the coarse-graining algorithm from Schubert and Rath (2021) instead of doing these calculations in spherical coordinates.

3. Results and discussion

a. The formation of Brazil Current meanders

To analyze the occurrence of horizontal shear instabilities associated with BC meanders, we use a CST cyclone event that started in September 2016 of the CROCO simulation. On 12 September 2016, we observe an incoming westward-propagating anticyclone at about 22°S 37.5°W, and a fully formed CST cyclone at about 23°S, 39.75°W (Fig. 2a). As the anticyclone approaches the continental slope, the former CST cyclone is displaced offshore and a secondary BC bump starts to be generated at about 22.15°S, 40°W (Fig. 2b). The anticyclone keeps interacting with the continental slope, and the bump evolves into a second CST cyclone at about 23°S, 40.5°W (Fig. 2c).

This event displays a typical configuration of upstream-anticyclone and downstream-cyclone observed off CST (Mill et al. 2015; Pereira et al. 2019). Furthermore, altimetry observations confirm that CST cyclones can be generated after incoming anticyclones reach the continental slope. For instance, Figs. 2d–f displays horizontal distributions of streamfunction (ψ) and geostrophic velocities (\mathbf{u}_g) data from the Sea Level Thematic Center [SL-TAC; distributed by Copernicus Marine Service (CMEMS)] during the formation of a CST eddy in 2006.

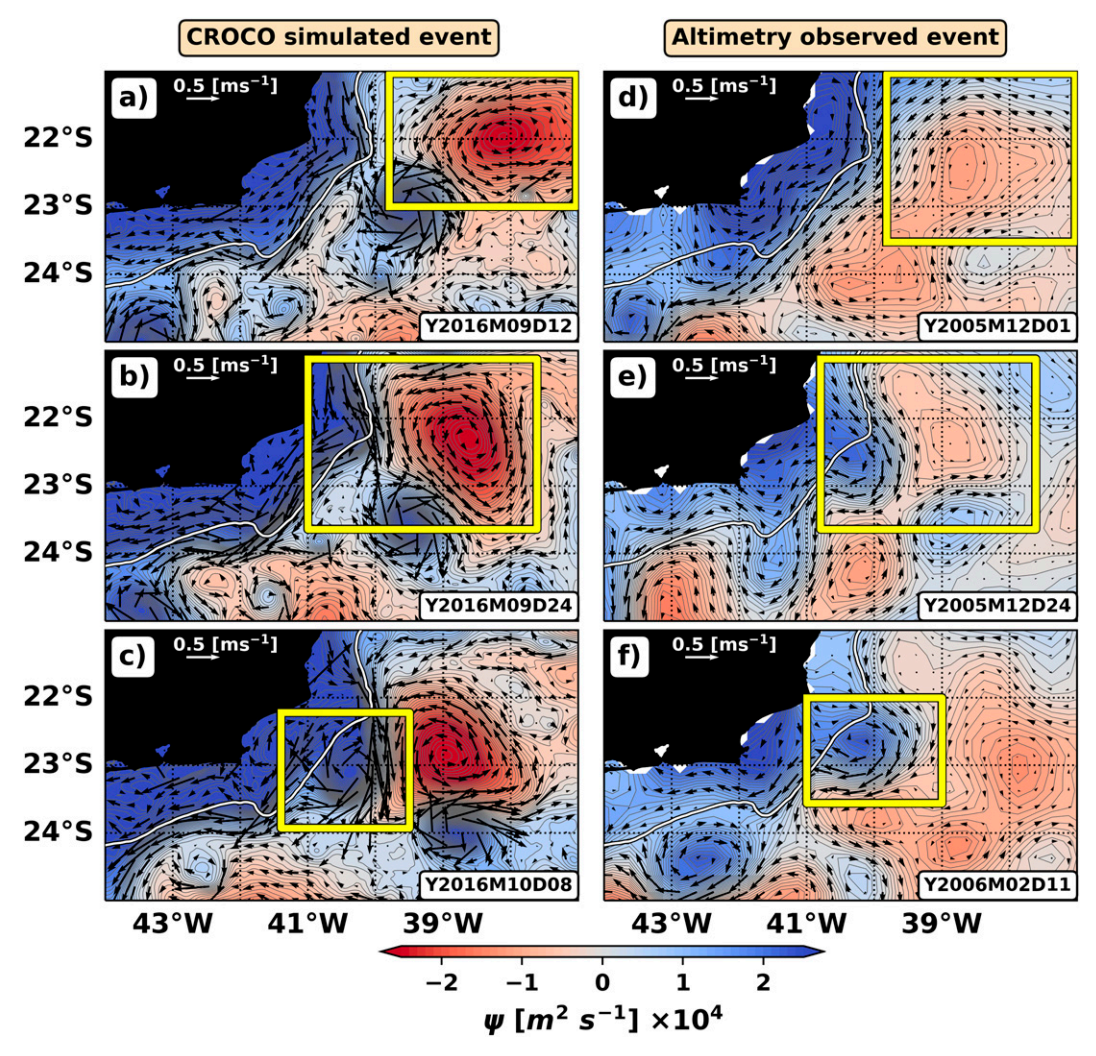


FIG. 2. The arrival of incoming anticyclones and the formation of CST eddies as depicted by streamfunction (ψ) and geostrophic velocity (\mathbf{u}_g) maps derived from sea surface height data from (left) a CROCO simulated event and (right) an altimetry observed event. Yellow boxes display snapshots of (a),(d) the incoming anticyclone from the east; (b),(e) the anticyclone hitting the continental shelf break; and (c),(f) the formation of a CST eddy downstream. The 160-m isobath (solid white line) is shown to highlight the interaction of the incoming anticyclones with the shelf break. Regions shallower than 160 m should be analyzed with caution in (d)–(f) due to the limitations of altimetry data within the shelf.

In the CROCO simulation, when the incoming anticyclone of September 2016 reaches the continental slope upstream of 22.2°S, the cyclonic vorticity increases and Ro reaches $\mathcal{O}(1)$ values (Fig. 3a; maps are shown at 160-m depth, close to the shelf break, as the shear instabilities are more frequently observed in this region). The CST cyclone is generated subsequently when the amplified cyclonic vorticity is shed to the ocean interior (Fig. 3b). The anticyclone keeps interacting with the slope and ejects strong cyclonic filaments that feed the CST eddy and contribute to its growth. By 8 October 2016, we observe a submesoscale cyclone and a belt of intense vorticity inside the mesoscale meander (Fig. 3c). Eventually, a second submesoscale cyclone is formed and additionally contributes to the CST cyclone growth (Fig. 3d). Figure 4a shows the isopycnal and velocity structure of the meso- and

submesoscale cyclones (blue transect from Fig. 3d). The two submesoscale cyclones span the upper 600 m and have radii of \sim 20 km. They present associated $\mathcal{O}(1)$ Ro and generate 50–100 m day⁻¹ vertical velocities, but the associated Richardson number (Ri) does not reach $\mathcal{O}(1)$ values (Figs. 4b–d).

The amplification of the cyclonic vorticity (Ro \sim 2) adjacent to the bottom boundary spans, approximately, from 100- to 300-m depth during the event (Figs. 5a–d). Consequently, fq is injected near the bottom exceeding 5×10^{-13} s⁻⁴ values (Figs. 5e–h). Note that the amplification of both properties occurs where the anticyclone squeezes the BC against the slope and, consequently, increases the horizontal shear (Figs. 5e–h).

We perform an energy analysis to verify if barotropic shear instability is involved in this process. The energy conversion terms are integrated between 100 and 300 m as the amplification

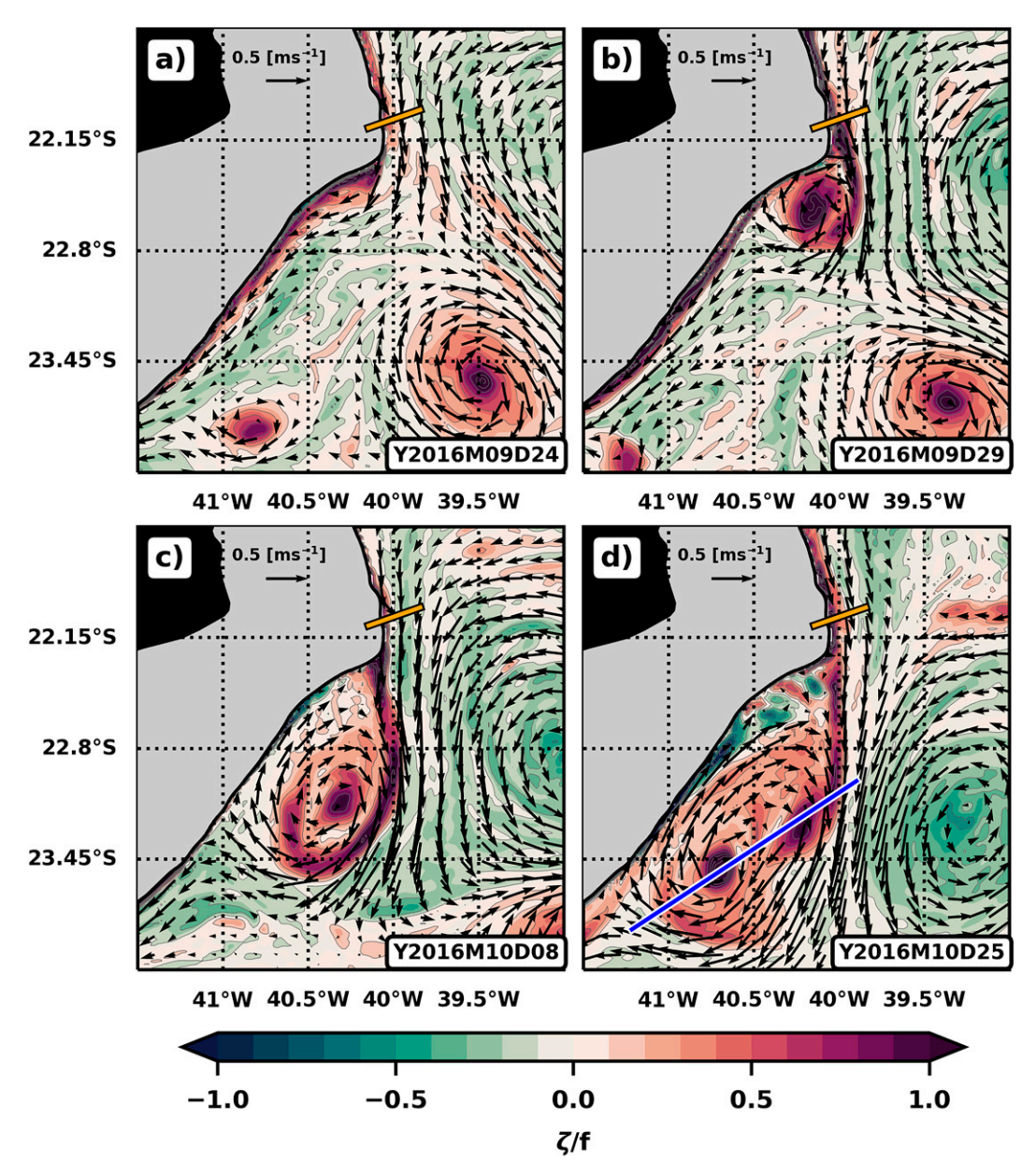


FIG. 3. (a)–(d) Horizontal distributions of ζ/f and horizontal velocities at 160-m depth during a CST cyclone event in September–October 2016. The blue and orange lines display the positions of the vertical sections shown in Figs. 4 and 5, respectively.

of Ro and fq occurs in this region. Our results show that the vertically integrated HSP is positive at about 22.25°S, 40.1°W where the incoming anticyclone interacts with the slope (Figs. 6a–c). Thus, similar to the Gulf Stream case (Gula et al. 2016a), barotropic instability indeed ejects cyclonic filaments and SCVs that contribute to the growth of mesoscale meanders downstream. This explains why the submesoscale cyclones do not reach O(1) Ri. Their generation through barotropic shear instability does not involve a reduction of the stratification.

Downstream of 22.25°S, 40.1°W, the BP and BF terms are positive in some regions within the mesoscale cyclones (Figs. 6d–h).

Thus, in accordance with da Silveira et al. (2008, 2023), Rocha et al. (2014), and Magalhães et al. (2017), our analysis demonstrates that baroclinic instability occurs during the growth of the BC meanders. We observe that BP and BF can also be positive (but not as high as HSP) at about 22.25°S, 40.1°W. Thus, even though barotropic instability is dominant near the separation point since the HSP term is larger, baroclinic instability also has some importance.

Although prone to baroclinic instability from 20° to 36°S (Magalhães et al. 2017), BC cyclones are favorably triggered off CST due to (i) the arrival of mesoscale anticyclones upstream of separation regions and (ii) the subsequent

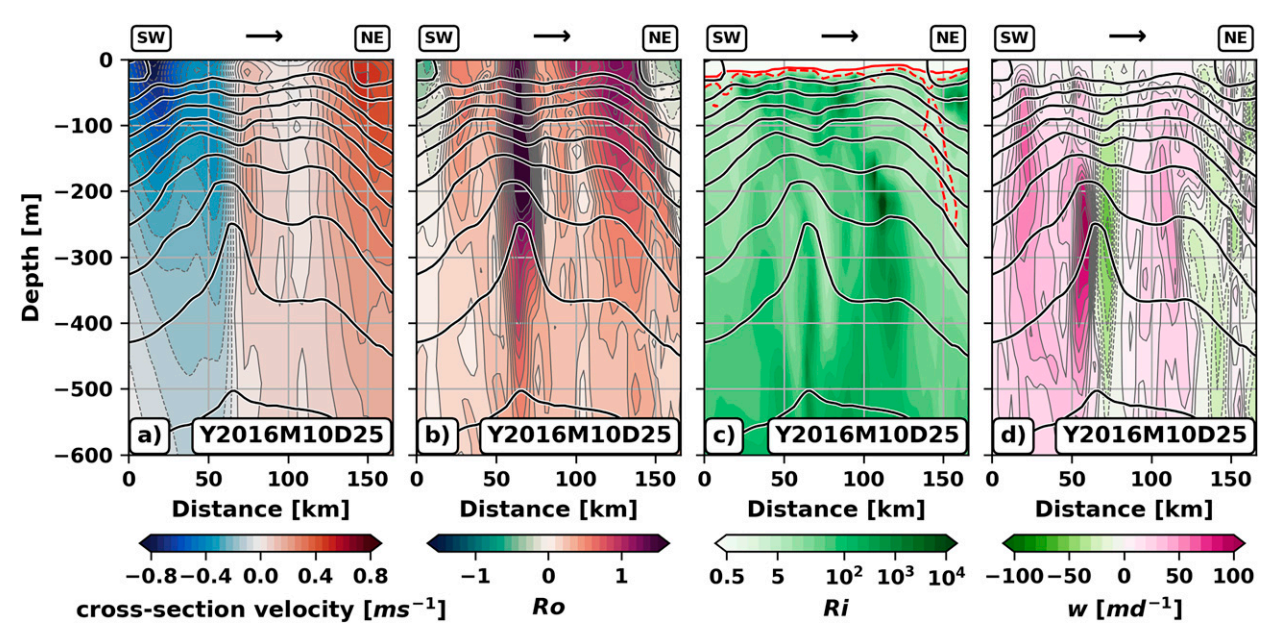


FIG. 4. Vertical sections of (a) cross-section velocities, (b) Rossby number, (c) Richardson number in log scale, and (d) vertical velocities at the blue transect from Fig. 3d. Black solid contours show isopycnals. Red solid and dashed contours in (c) show the lower and upper limits (0.5 and 5), respectively, of $\mathcal{O}(1)$ Richardson number. Section orientations are shown above the panels.

generation of barotropic instability that triggers the meander formation. The same process is observed during the formation of CF cyclones downstream of 23°S (not shown).

b. The submesoscale-to-mesoscale inverse cascade

In the previous subsection, we have shown that barotropic instability can be responsible for triggering the formation of BC meanders off the capes. In addition, we have shown that such instabilities shed cyclonic filaments and submesoscale cyclones into the mesoscale meanders. In this section, we aim to answer if these submesoscale features contribute to the growth of the meanders in a submesoscale-to-mesoscale inverse cascade.

We analyze the kinetic energy flux across scales using a coarse-graining approach (Aluie et al. 2018; Schubert et al. 2020, 2021). We adopt $L=2R_d=50$ km as the transition scale between submesoscale and mesoscale flows for the region (Houry et al. 1987). Figure 7 shows the KE fluxes through L=50 km at 160-m depth in the same CST cyclone event displayed in Fig. 3.

We observe that, after the formation of the CST cyclone, the KE fluxes are predominantly upscale inside the mesoscale meander (Fig. 7). The most intense values (\sim -1 \times 10⁻³ mW m⁻² km⁻¹) are observed on 25 October 2016 (Fig. 7d) when there are two submesoscale cyclones within the eddy [one at about 23.4°S, 40.75°W, and the other at about 23.6°S, 40.25°W; Fig. 3d)]. Therefore, the submesoscale features shed by barotropic instability contribute to the growth of the BC meanders in a submesoscale-to-mesoscale inverse cascade. This is similar to the California Undercurrent case, where inertial instability sheds filaments and submesoscale coherent vortices (SCVs) that contribute to the growth of anticyclones downstream of a separation region (Molemaker et al. 2015).

Subject to the limitations of interpretation of the fluxes close to the boundaries, we observe that KE fluxes are predominantly downscale where the CST cyclone interacts with the slope (Fig. 7d). This is a region where the shear between the eddy and the slope increases anticyclonic vorticity and leads Ro to $\mathcal{O}(1)$ values (Fig. 3d). As anticyclonic vorticity is increased, (1 + Cu)fq can become negative and lead to inertially/symmetrically unstable flows. These instabilities contribute to the forward cascade of energy (Gula et al. 2016b), which is in accordance with the downscale KE fluxes found in the region. In the next subsection, we address the occurrence of these instabilities and their association with the generation of anticyclonic SCVs.

c. Submesoscale anticyclones generation

After their formation, the BC meanders often grow quasistationarily adjacent to the shelf break (da Silveira et al. 2008). In sections 3a and 3b, we have shown that during this process, the shear between the cyclones and the topography increases anticyclonic vorticity and generates downscale KE fluxes. In this section, we aim to answer if this process is associated with the development of inertial/symmetric instabilities and, subsequently, with the generation of anticyclonic SCVs (e.g., Molemaker et al. 2015; Morvan et al. 2019; Napolitano et al. 2021b; Lazaneo et al. 2022).

We start by analyzing the temporal evolution of Ro on a CST cyclone event at 450 m depth (March 2019 of the simulation). As in the cases mentioned before, we observe that the shear between the inshore limb of the mesoscale meander and the slope amplifies anticyclonic vorticity, and leads the Ro to $\mathcal{O}(1)$ values (Fig. 8a). After some days, we observe that filaments of amplified anticyclonic vorticity are ejected offshore

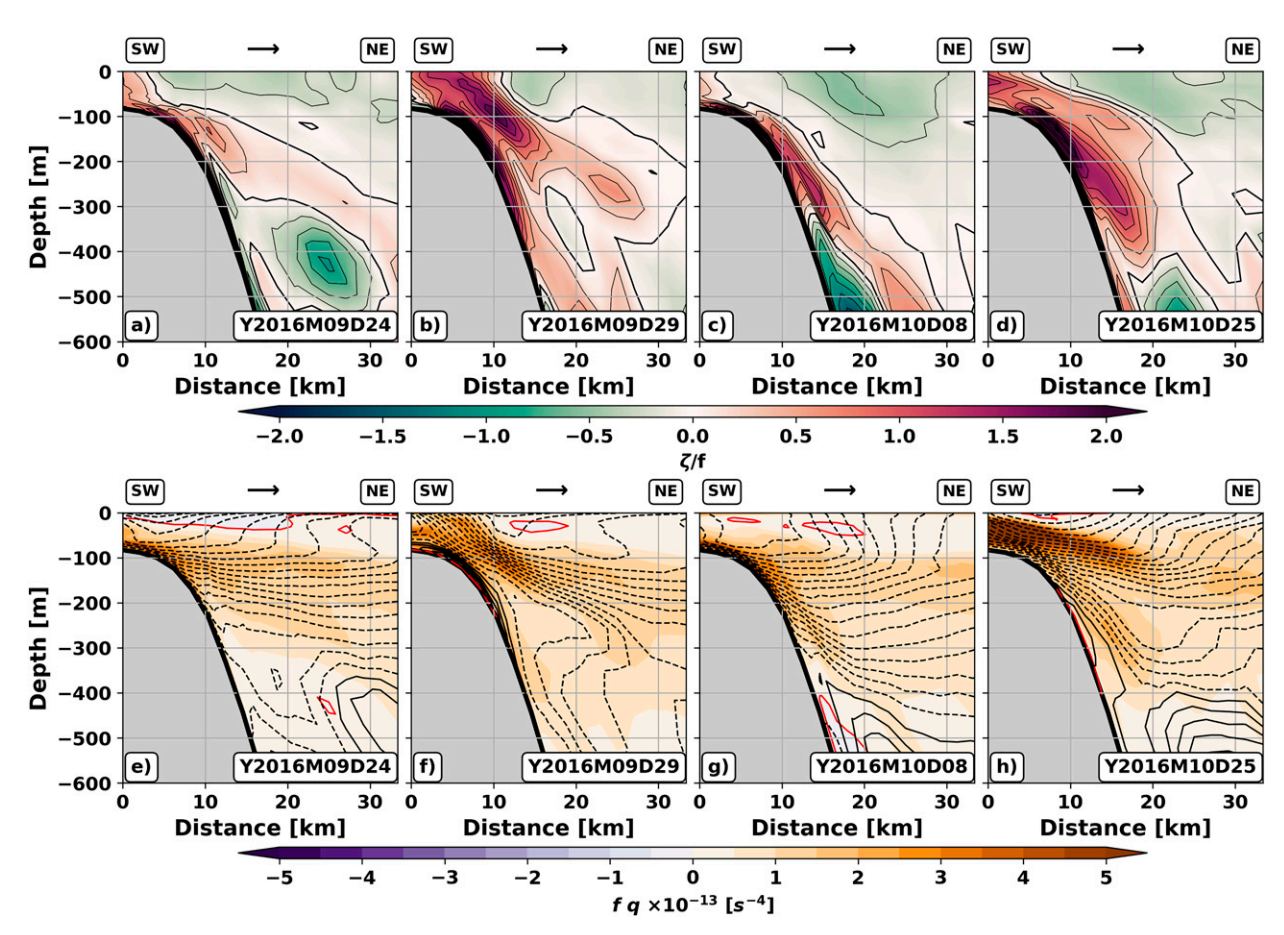


FIG. 5. (a)–(d) Vertical sections of $\zeta I f$ at the orange transects from Fig. 3 during the CST cyclone event. (e)–(h) Similarly, vertical sections of fq during the CST cyclone event. Isotachs are shown in (e)–(h), with positive (negative) values represented by solid (dashed) isolines. Red isolines are fq = 0 contours. Section orientations are shown above the panels.

and roll-up into anticyclonic SCVs (Figs. 8b,d). One of the generated SCVs is advected southward and orbits the whole periphery of the mesoscale meander until reaching the slope (Figs. 8b-f), while the other is advected northward (Figs. 8d,e).

Next, we address the stability of the flow during the SCV generation. Figures 9a–c show that fq is negative in the region where the filaments are ejected and within the SCVs for some days before becoming marginally stable. This indicates that the flow is unstable to either symmetric, inertial, or gravitational instabilities during the formation of the SCVs.

Buckingham et al. (2021b) show that in low-stratified waters [Ri O(1)] with high curvature [Cu O(1)], cyclones can become strongly unstable and anticyclones can become marginally stable. Figures 10a, 10b, 10d, and 10e show that Cu and Ri reach O(1) between 22.45°–22.25°S and 40.4°–39.9°W. Thus, we also examine the stability of the flow using the generalized Rayleigh criterion which considers centrifugal effects (Figs. 9d–f).

Indeed, part of the anticyclonic flow is stabilized in the region where the filaments are ejected when considering centrifugal effects (cf. the area between 22.45°–22.25°S and

 40.4° – 39.9° W on Figs. 9a,d, for example). Because of curvature, instability occurs in slightly different regions than those obtained with the fq criterion. However, these differences are small and become unimportant as the SCVs propagate away from topography since Ri is generally low only near the boundary. Thus, our results show that centrifugal forces play a marginal role. Nonetheless, we choose to still use the most generalized criterion in our analyses.

To verify the vertical extent of the unstable regions, we analyze vertical sections of (1 + Cu)fq, Ro and Ri throughout the SCV generation and propagation process (the positions of the vertical sections are depicted on Fig. 8). Figures 11a-c show that the shear between the CST cyclone and the slope generates a region of negative (1 + Cu)fq, $\mathcal{O}(1)$ Rossby number, and $\mathcal{O}(1)$ Richardson number between 100 and 900 m. According to the gradient wind Thomas angle (Buckingham et al. 2021a), the flow is symmetrically and inertially unstable in this area (Fig. 11d). Corroborating Wenegrat et al. (2018) and Wenegrat and Thomas (2020), we observe that a mix of inertial and symmetric instability occurs where topography is sharply sloped whereas symmetric instability occurs where the sloped topography flattens.

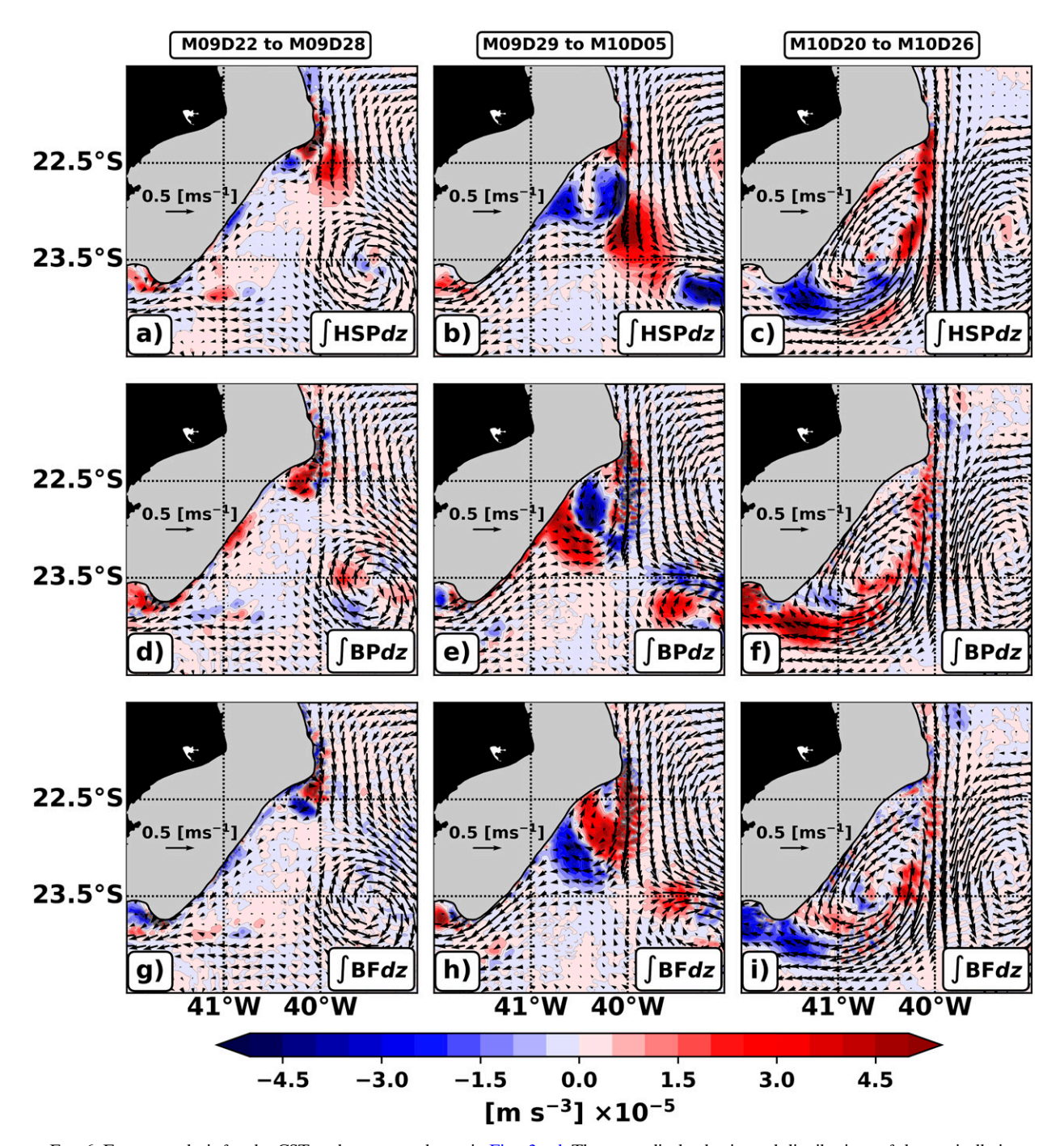


FIG. 6. Energy analysis for the CST cyclone event shown in Figs. 3a–d. The maps display horizontal distributions of the vertically integrated (100–300 m) (a)–(c) HSP, (d)–(f) BP, and (g)–(i) BF. Vectors represent the vertically averaged (100–300 m) horizontal velocities. (left) The period between 22 and 28 Sep, (center) the period between 29 Sept and 5 Oct, and (right) the period between 20 and 26 Oct.

The anticyclonic SCV that migrates south spans from 100 to 700 m with radii between 10 and 15 km (Figs. 11e-h). It remains symmetrically and inertially unstable for some days after its generation. After that, it becomes marginally stable but still retains its convex-lens-shaped isopycnals and its $\mathcal{O}(1)$ Ro values (Figs. 11i-l).

The southward migrating SCV is rapidly destroyed since it hits the continental slope. By contrast, the northward migrating SCVs can trigger the formation of subsurface mesoscale anticyclones (Fig. 12). In particular, we observe this process occurring during an event of northward migration of the CST eddy in April 2019. Such migrating events were described by

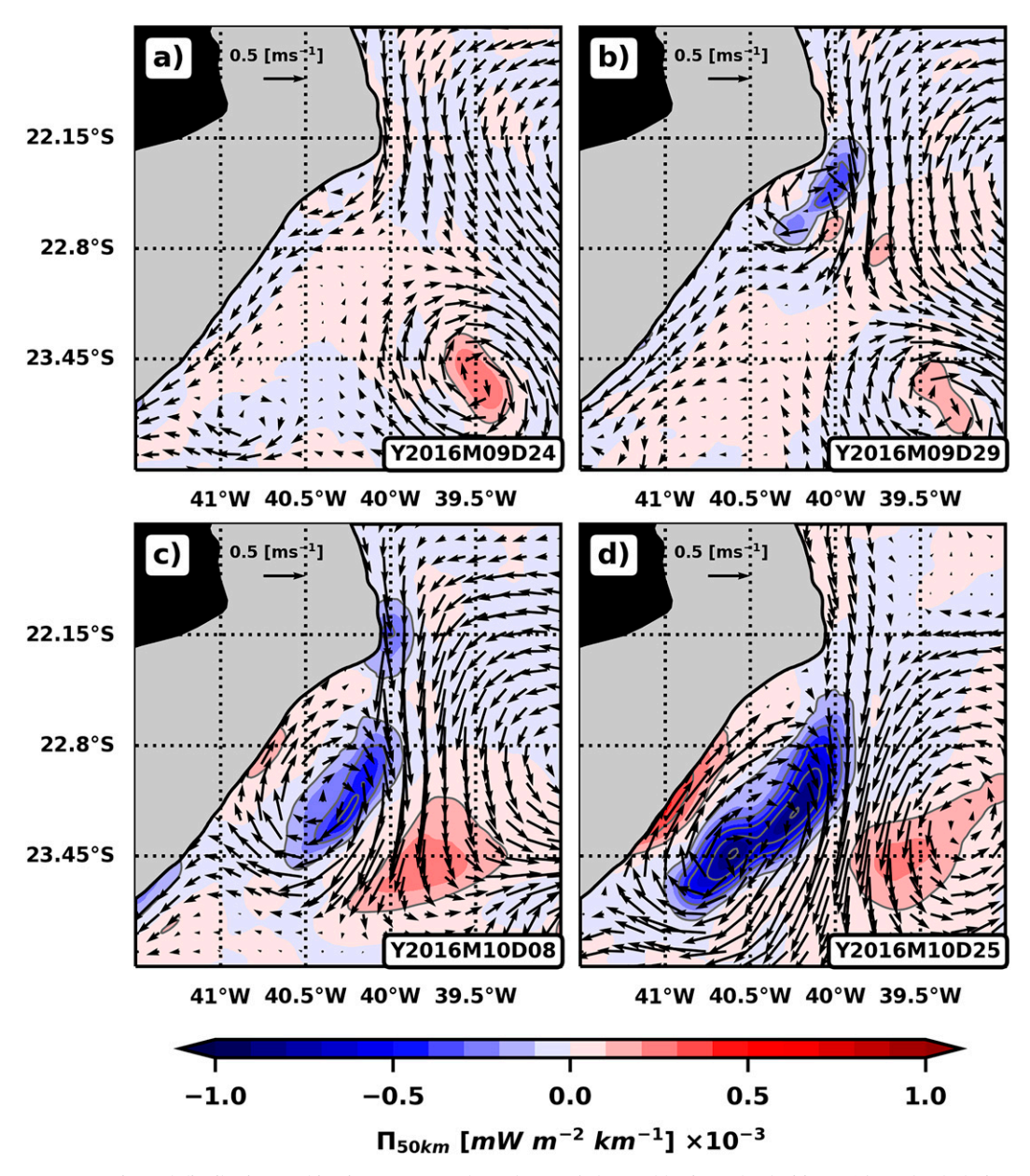


FIG. 7. Horizontal distributions of kinetic energy flux through $L=50~\mathrm{km}$ and horizontal velocities at 160-m depth during a CST cyclone event.

Mill et al. (2015), who estimated that approximately 20% of the CST cyclones translate north. Figures 12a, 12b, 12d, and 12e show the northward migrating SCV from Fig. 8e being advected at 450 m depth and keeping its low (1 + Cu)fq signature. However, as the CST cyclone starts to migrate north, the interaction with the slope generates a second strong and unstable anticyclonic SCV that cascades \sim 0.25 mW m⁻² km⁻¹ of KE downscale through L = 50 km (Figs. 12b,e,h). Subsequently, this SCV grows into a subsurface mesoscale anticyclone with a radius of \sim 30 km (Figs. 12c and 13a). This anticyclone presents associated $\mathcal{O}(1)$ Ro and Ri numbers (Figs. 12c and 13b,c), as well as regions of flow instability

(Figs. 12f and 13d). Finally, we observe that KE is fluxed both up- and downscale inside the mesoscale anticyclone (Fig. 12i). This occurs because the submesoscale features inside the eddy contribute to (i) the inverse cascade of energy by playing a role on the growth of the anticyclone and (ii) the forward cascade of energy due to the instability of the flow. However, we remark once again, that results that are over a distance of 25 km from the boundary are subject to the uncertainty of the method application close to boundaries.

In summary, our results indicate that anticyclonic SCVs can be generated by the interaction of BC meanders with the continental margin. These SCVs are triggered by inertial/symmetric

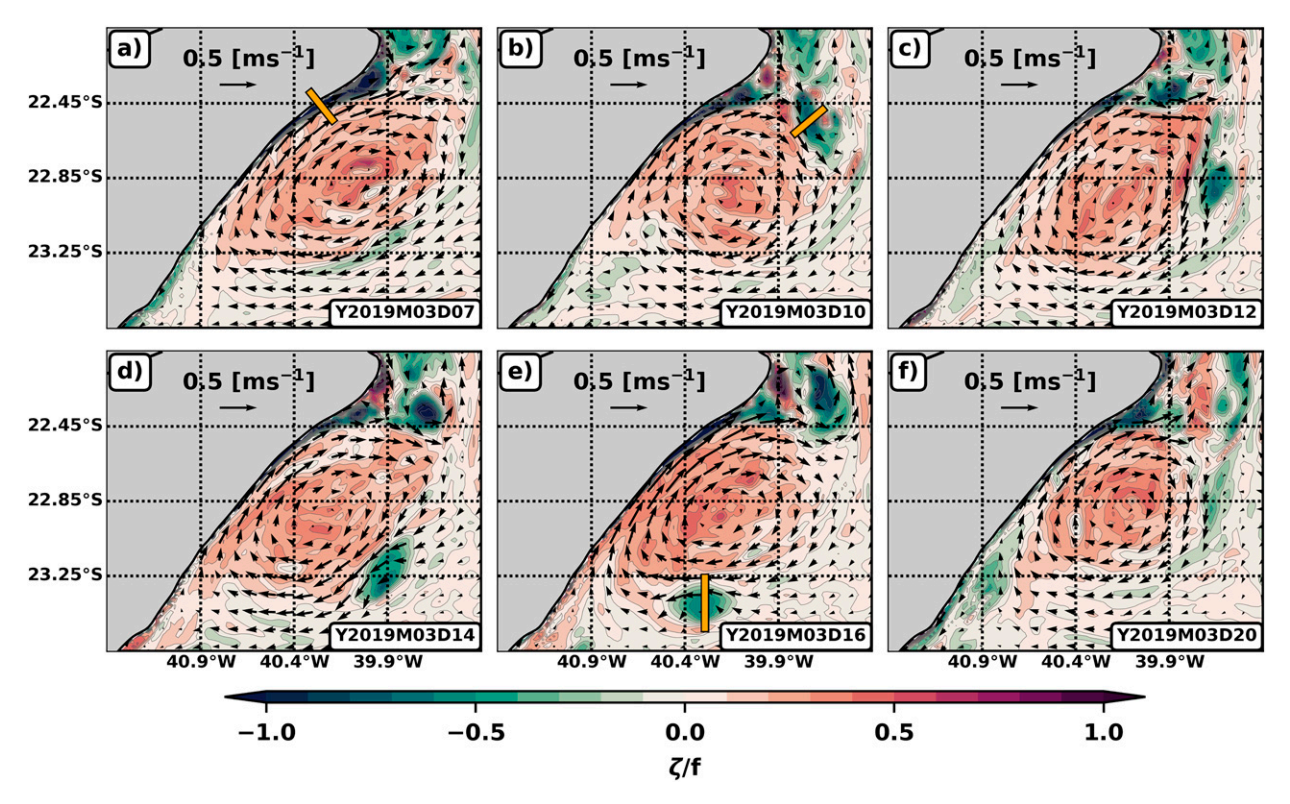


FIG. 8. Horizontal distributions of ζ/f and horizontal velocities at 450 m during a CST cyclone event in March 2019. Orange lines display the positions of the vertical sections shown in Fig. 11.

instability and remain with negative/low (1 + Cu)fq waters for several days. Some can evolve into mesoscale eddies, while others can be destroyed since they hit the western boundary. The lifetime of these SCVs is smaller than those advected by the large-scale flow in the interior ocean (e.g., Dewar and Meng 1995; Lazaneo et al. 2022). However, they play an important role in cascading energy to both larger and smaller scales. In fact, Lazaneo et al. (2022) observed that anticyclonic SCVs can lead to KE dissipation in the interior ocean. Therefore, the SCVs described here may constitute an important sink of energy for the BC.

4. Summary and conclusions

In this study, we use a submesoscale-permitting CROCO simulation to investigate submesoscale shear instabilities associated with BC cyclones generated between 22° and 23°S. Our results indicate that the arrival of anticyclones upstream of the CST can ignite barotropic instability from 100 to 300 m and, consequently, can trigger the formation of CST cyclones downstream. The same process can occur during the formation of CF cyclones downstream of 23°S (not shown). The shear between the incoming anticyclones and the slope keeps generating barotropic instability and ejects amplified cyclonic filaments and submesoscale vortices offshore. Such submesoscale features feed the mesoscale meanders and contribute to their growth in a submesoscale-to-mesoscale inverse cascade (e.g., Molemaker et al. 2015). The submesoscale cyclones

span the upper 600 m with radii of \sim 20 km, present $\mathcal{O}(1)$ Ro, and yield 50–100 m day⁻¹ vertical velocities. Thus, their impact on the vertical exchange of tracers and the biogeochemical dynamics within the BC meanders is a topic that should be addressed in future studies.

After their generation, BC meanders trigger inertial and symmetrical instabilities adjacent to the slope. Between 100and 900-m depth, the interaction of the inshore limb of the cyclones with the slope increases the shear, amplifies anticyclonic vorticity, and reduces the Richardson number to $\mathcal{O}(1)$ values. This leads to (1 + Cu)fq < 0, then the flow becomes inertially and/or symmetrically unstable. Subsequently, anticyclonic filaments are ejected offshore and roll up into anticyclonic SCVs. These anticyclonic SCVs present a smaller lifetime than those generated in the interior ocean (e.g., Lazaneo et al. 2022). However, they cascade energy to both larger and smaller scales. Some can evolve into subsurface mesoscale eddies, while others remain marginally stable until being destroyed by the topography. SCVs can generate pathways to energy dissipation (Lazaneo et al. 2022). Therefore, despite having short life cycles, the SCVs described here can be relevant to the sink of energy within ocean western boundaries.

By using a submesoscale-permitting simulation we were able to show different submesoscale processes that arise from flow-topography interactions associated with the BC meanders. However, some caveats arise due to simulation horizontal and vertical resolutions. We list them as follows:

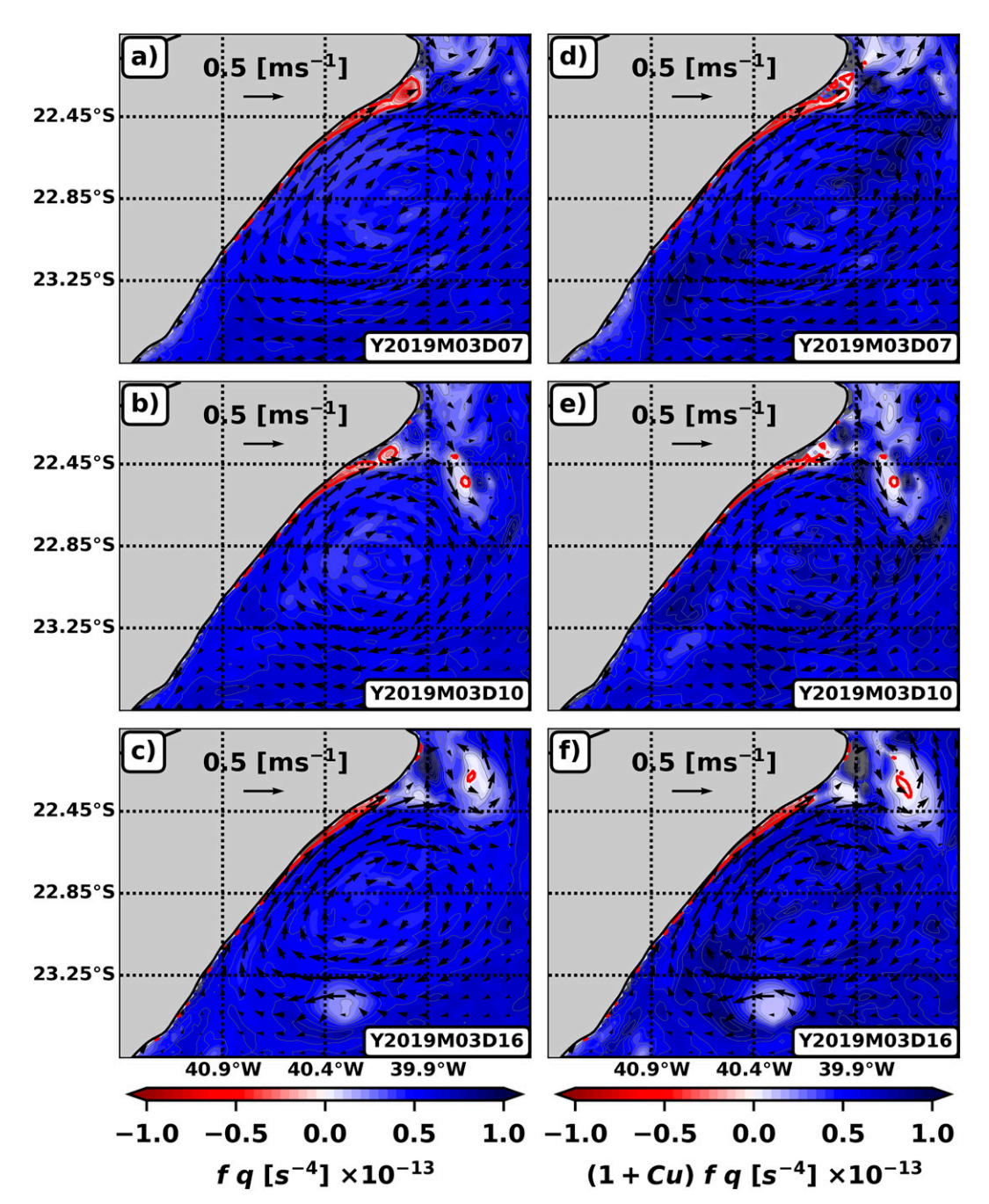


FIG. 9. Horizontal distributions of (a)–(c) fq, (d)–(f) (1 + Cu)fq, and horizontal velocities at 450-m depth during a CST cyclone event in March 2019. Red solid lines show fq = 0 and (1 + Cu)fq = 0 contours.

- Inability to fully resolve submesoscale instabilities: As we use a ~2-km horizontal resolution, our simulation is able to capture the fronts and regions that become symmetrically, inertially and gravitationally unstable. However, it needs to parameterize these instabilities using the KPP scheme as they develop at scales of 10 m-1 km (e.g., Dong et al. 2021);
- 2) Lack of accuracy in number and intensity of SCVs formed: While other studies have also used 2-km resolution
- simulations to study the formation of SCVs (e.g., Vic et al. 2015), increasing the horizontal resolution can lead to a marked increase in the number and strength of SCVs generated (e.g., Molemaker et al. 2015);
- Lack of accuracy in resolving the BBL dynamics: SCV generation as well as the evolution of symmetric and inertial instabilities near the bottom are strongly linked to the BBL dynamics (Molemaker et al. 2015; Srinivasan et al.

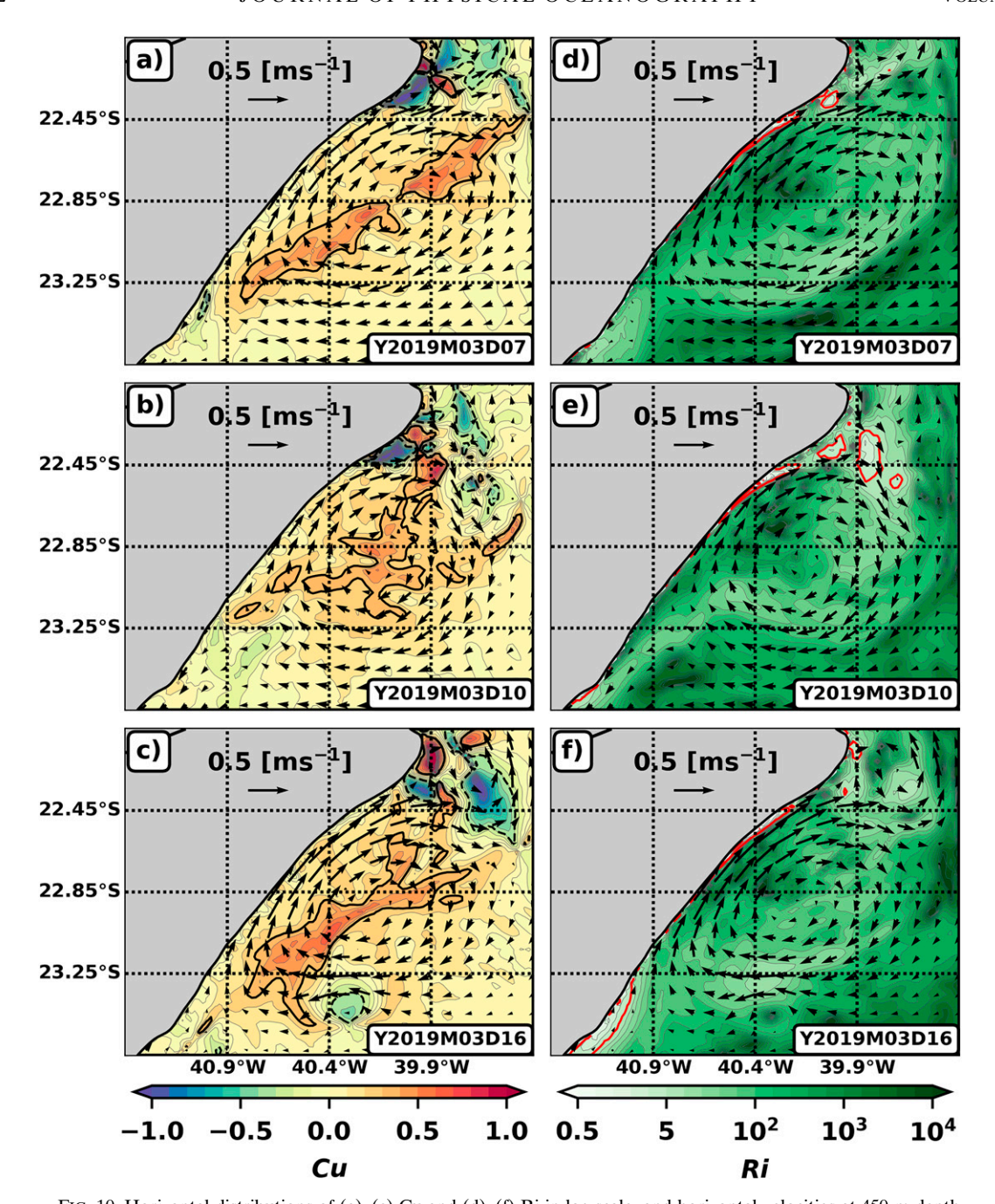


FIG. 10. Horizontal distributions of (a)–(c) Cu and (d)–(f) Ri in log scale, and horizontal velocities at 450-m depth during a CST cyclone event in March 2019. Black solid (dashed) lines in (a)–(c) show 0.3 (-0.3) Cu contours. Red solid and dashed contours in (d)–(f) show the lower and upper limits (0.5 and 5), respectively, of $\mathcal{O}(1)$ Richardson number.

2019; Wenegrat and Thomas 2020) and, thus, is strictly dependent on how well this layer is resolved. In this work, we only resolve 1–2 cells within the BBL (e.g., Fig. 11d).

Further simulations using higher horizontal and vertical resolutions need to be performed to better resolve BBL processes impacting the SCVs generation, and the submesoscale

instabilities that develop from the interaction of the BC meanders with topography. Nevertheless, this work represents a first attempt to assess the role of smaller-scale dynamics in the BC quasi-stationary meanders.

The regional BC mesoscale cyclones impact coastal upwelling, cross-shelf water transport, and biogeochemical dynamics (Calado et al. 2010; Palóczy et al. 2014; Mill et al. 2015;

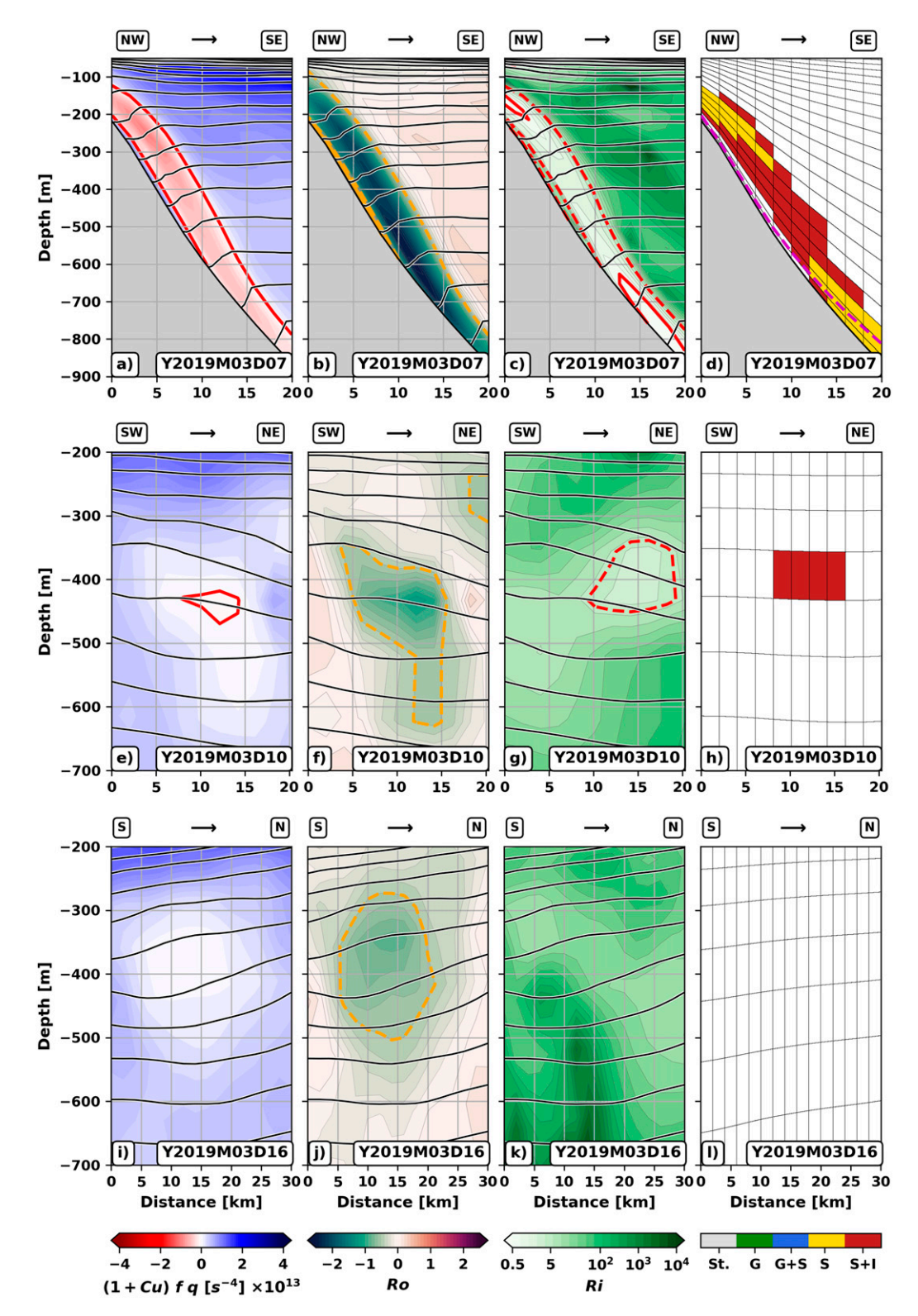


FIG. 11. Vertical sections of (first column) (1 + Cu)fq, (second column) the Rossby number, (third column) the Richardson number in log scale, and (fourth column) the instability category at the yellow transect from (a)–(d) Fig. 8a, (e)–(h) Fig. 8b, and (i)–(l) Fig. 8e. Black solid contours show isopycnals. Red solid contours in the first column show the (1 + Cu)fq = 0 contour. Yellow dashed contours in the second column show the Ro = -0.5 contour. Red solid and dashed contours in the third column show the lower and upper limits (0.5 and 5), respectively, of $\mathcal{O}(1)$ Richardson number. The pink dashed line in (d) shows the depth of the bottom boundary layer. Section orientations are shown above the panels.

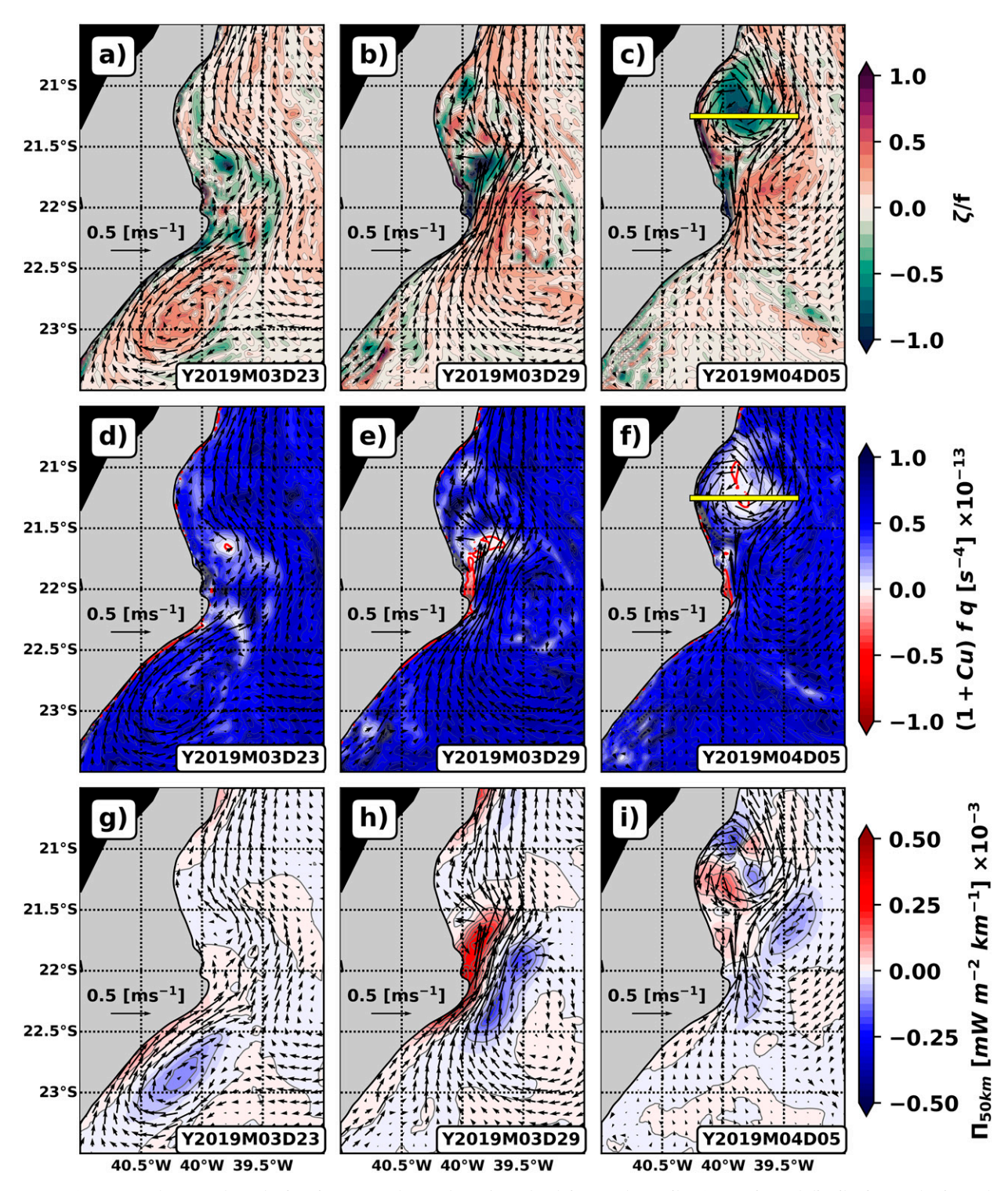


FIG. 12. CST cyclone northward migration event observed at 450-m depth in March-April 2019. Horizontal distributions of horizontal velocities and (a)–(c) ζ/f , (d)–(f) (1 + Cu)fq, and (g)–(i) kinetic energy flux through L=50 km. The red solid isolines in the second row show (1 + Cu)fq=0 contours, and the yellow solid lines in (c) and (f) show a transect crossing the mesoscale anticyclone (Fig. 13).

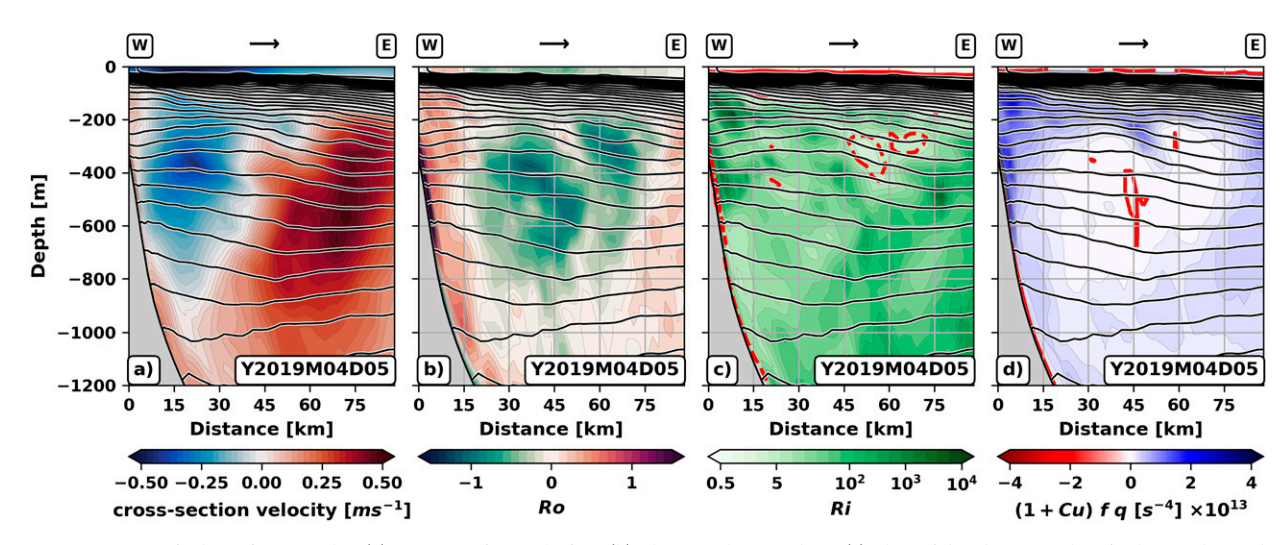


FIG. 13. Vertical sections of the (a) cross-section velocity, (b) the Rossby number, (c) the Richardson number in log scale, and (d) (1 + Cu)fq at the black transect crossing the mesoscale anticyclone displayed in Figs. 12c and 12f. Black solid contours show isopycnals. Red solid and dashed contours in (c) show the lower and upper limits, respectively, of $\mathcal{O}(1)$ Richardson number. Red solid isolines in (d) show the (1 + Cu)fq = 0 contour.

Pereira et al. 2019). We have shown that submesoscale shear instabilities can play a role in the formation of these mesoscale meanders and the generation of associated submesoscale vortices. However, further studies need to address whether the ejection of filaments and SCVs by barotropic instability is the main triggering mechanism of the BC meanders or not. We are currently working to address (i) the origin of the anticyclones that trigger barotropic shear instability upstream of CST and CF and (ii) the impact of submesoscale motions on the biogeochemical dynamics within the BC cyclones.

Acknowledgments. C. D. Luko acknowledges support from FAPESP (2020/04124-0), and CNPq (130288/2020-9). C. Z. Lazaneo acknowledges support from CAPES (Finance Code 001), and CNPq (205857/2018–3). I. C. A. da Silveira acknowledges support from CNPq (442926/2015-4 and 307814/2017-3), CAPES (88882.158621/2014-01), and FAPESP (2015/21729-4). F. Pereira acknowledges support from FAPESP (2017/15026-6). A. Tandon acknowledges support from NSF-OCE (1755313 and 2148404) and ONR (N00014-17-1-2355 and N00014-18-1-2799). C. D. Luko also acknowledges Prof. Christian Buckingham for participating on the defense committee from the Master's thesis that generated this manuscript, as well as Tiago Bilo and Iury Simoes-Sousa for the Li et al. (2006) Python code. The authors also thank the reviewers for all suggestions and comments that helped to improve this manuscript.

Data availability statement. The CROCO code used to run the simulation is publicly available at https://www.croco-ocean.org/. The ERA5 atmospheric forcing and the TPX07 tide forcing code are publicly available at https://cds.climate.copernicus.eu/ and https://www.croco-ocean.org/download/datasets/, respectively. The GLORYS12V1 daily reanalysis used for the model initial and boundary conditions as well as the altimetry data used to show that the simulation results

match the observations are publicly available at http://www.marine.copernicus.eu. The WOA18 climatology is publicly available at https://www.ncei.noaa.gov/access/world-ocean-atlas-2018/. The GEBCO2021 data are publicly available at https://www.gebco.net/. The code from Schubert and Rath (2021) used for the coarse-graining approach is publicly available at https://doi.org/10.5281/zenodo.4486265. The code used to employ the Li et al. (2006) method is publicly available at https://github.com/iuryt/vector_fields.

APPENDIX

Model Evaluation

The simulation is evaluated by comparing the mean thermohaline and velocity structure with available data and reports from previous studies. We use the post-spinup period of 2016-19 to construct the model temporal averages. Figure A1a shows the annual mean temperature and salinity (TS) diagrams from the simulation and the World Ocean Atlas 2018 (WOA18) climatology. We compute both TS averages within the area of interest (red dashed box on Fig. 1). Results show that the simulation represents well the regional thermohaline mean structure observed in the WOA18 climatology. Figure A1b shows the mean cross-section velocity vertical section at the black transect on Fig. 1. Corroborating Napolitano et al. (2019), we find that (i) the BC occupies the upper 200 m transporting \sim 2 Sv and reaches -0.5 m s⁻¹ at its surface core and (ii) the IWBC transports 13.1 Sv and reaches 0.2 m s^{-1} at its $\sim 800 \text{-m}$ core. Finally, we show that the simulation successfully represents CST and CF cyclones events (Fig. A2) as observed by Mill et al. (2015) and Pereira et al. (2019).

Last, we need to confirm that the simulation is submesoscale permitting. We examine snapshots and the probability

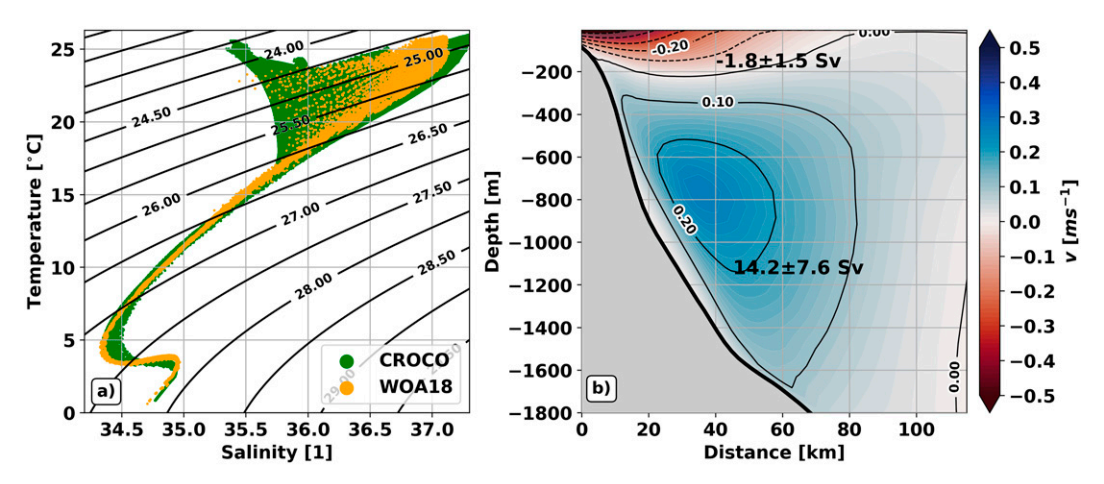


FIG. A1. (a) Temporal average of TS diagrams for the WOA18 climatology and the CROCO simulation computed within the area of interest (red dashed box on Fig. 1). (b) Temporal average of cross-section velocity at the black transect from Fig. 1.

density function (PDF) of the following properties (e.g., Napolitano et al. 2021b):

Rossby number =
$$Ro = \frac{\zeta}{f}$$
, (A1)

ND strain rate =
$$\frac{\alpha}{|f|} = \frac{\left[\left(\frac{\partial u}{\partial x} - \frac{\partial v}{\partial y} \right)^2 + \left(\frac{\partial v}{\partial x} + \frac{\partial u}{\partial y} \right)^2 \right]^{1/2}}{|f|}, \quad (A2)$$

ND divergence rate =
$$\frac{\delta}{|f|} = \frac{\frac{\partial u}{\partial x} + \frac{\partial v}{\partial y}}{|f|}$$
, (A3)

ND horizontal buoyancy gradient =
$$\frac{M^2}{f^2} = \frac{|\nabla_h b|}{f^2}$$
, (A4)

where ζ is the relative vorticity; f is the planetary vorticity; b is buoyancy; α is the strain; δ is the divergence; M^2 is the horizontal buoyancy gradient; ND stands for nondimensional; and u, v, and w are the zonal, meridional, and vertical velocity components, respectively.

The snapshots at 10 m and the correspondent PDFs of these properties reveal typical characteristics of submesoscale motions in accordance with Shcherbina et al. (2013) and Napolitano et al. (2021b) (Fig. A2). The Rossby number and the nondimensional strain and divergence rates reach $\mathcal{O}(1)$ values on the edges and in the center of the CST and CF cyclones (Figs. A2a-d). The Ro PDF shows large asymmetry with a typical tail toward cyclonic motions (skewness of 0.95; Fig. A2e), the divergence rate PDF shows a typical tail toward convergence (skewness of -0.44; Fig. A2g), and the strain rate PDF follows a χ^2 distribution (mean of 0.28 and skew of 2.92; Fig. A2f) with a tail of sporadic $\mathcal{O}(1)$ values. We observe that our simulation generates M^2f^{-2} extremes from 150 to 683 values, which correspond to M^2 values between 5 \times 10⁻⁷ and 2×10^{-6} s⁻² (Fig. A2h). These strong buoyancy gradients are in accordance with studies that investigate submesoscale motions (e.g., Thomas et al. 2016; McWilliams et al. 2019; Napolitano et al. 2021b). Hence, these results show that our simulation is indeed submesoscale permitting.

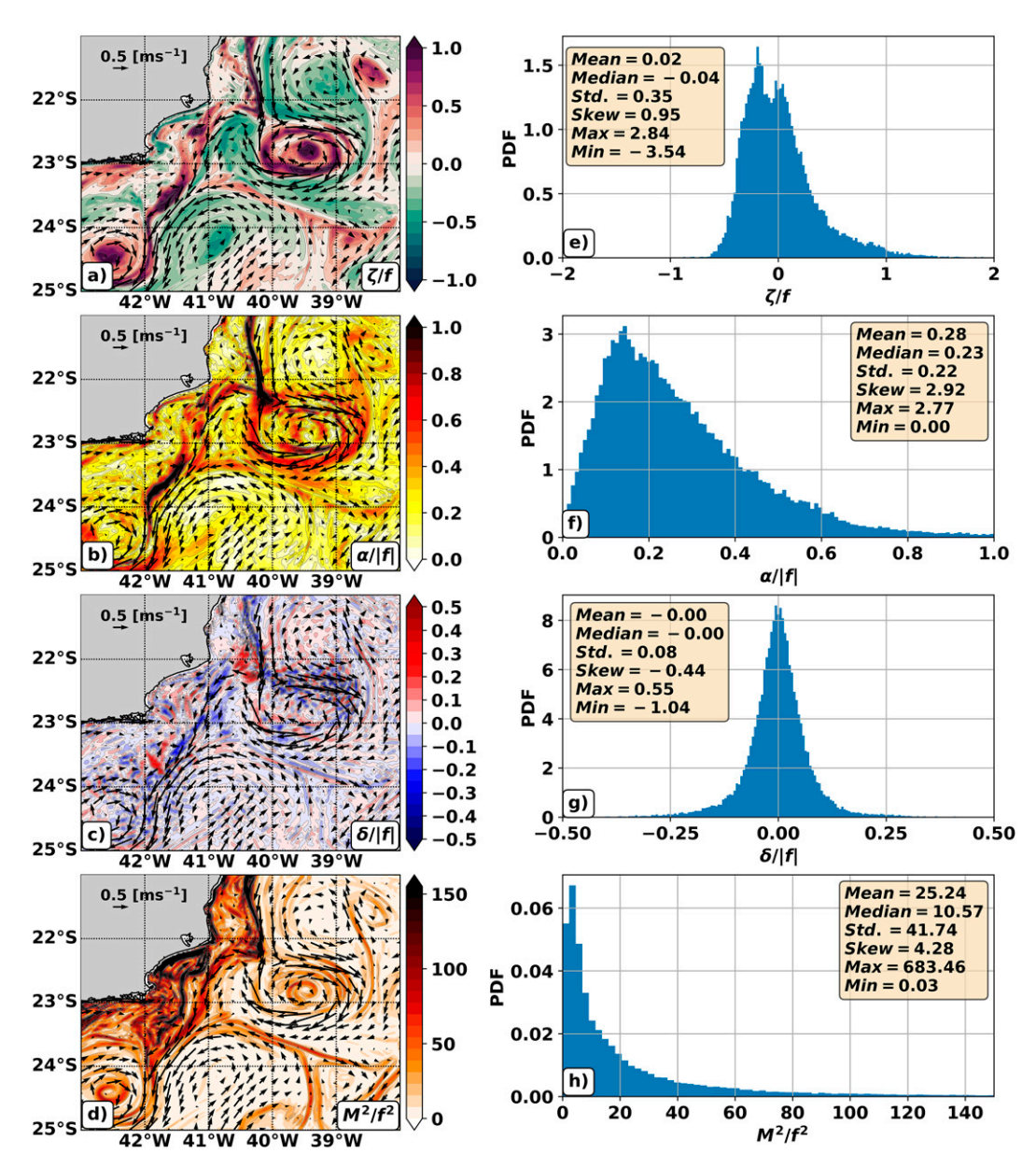


FIG. A2. (left) Horizontal distributions on 20 Mar 2017 at 10 m and (right) their respective PDFs of (a),(e) Ro, (b),(f) nondimensional strain rate, (c),(g) nondimensional divergence rate, and (d),(h) nondimensionalized horizontal buoyancy gradient. Horizontal velocities are also displayed in the horizontal maps in (a)–(d).

REFERENCES

Aluie, H., M. Hecht, and G. K. Vallis, 2018: Mapping the energy cascade in the North Atlantic Ocean: The coarse-graining approach. J. Phys. Oceanogr., 48, 225–244, https://doi.org/10. 1175/JPO-D-17-0100.1.

Balwada, D., Q. Xiao, S. Smith, R. Abernathey, and A. R. Gray, 2021: Vertical fluxes conditioned on vorticity and strain reveal submesoscale ventilation. *J. Phys. Oceanogr.*, 51, 2883– 2901, https://doi.org/10.1175/JPO-D-21-0016.1.

Buckingham, C. E., J. Gula, and X. Carton, 2021a: The role of curvature in modifying frontal instabilities. Part I: Review of theory and presentation of a nondimensional instability

criterion. *J. Phys. Oceanogr.*, **51**, 299–315, https://doi.org/10. 1175/JPO-D-19-0265.1.

—, —, and —, 2021b: The role of curvature in modifying frontal instabilities. Part II: Application of the criterion to curved density fronts at low Richardson numbers. *J. Phys. Oceanogr.*, **51**, 317–341, https://doi.org/10.1175/JPO-D-20-0258.1.

Calado, L., I. C. A. da Silveira, A. Gangopadhyay, and B. M. de Castro, 2010: Eddy-induced upwelling off Cape São Tomé (22°S, Brazil). Cont. Shelf Res., 30, 1181–1188, https://doi.org/ 10.1016/j.csr.2010.03.007.

Chen, R., G. R. Flierl, and C. Wunsch, 2014: A description of local and nonlocal eddy-mean flow interaction in a global

- eddy-permitting state estimate. *J. Phys. Oceanogr.*, **44**, 2336–2352, https://doi.org/10.1175/JPO-D-14-0009.1.
- da Silveira, I. C. A., L. Calado, M. Cirano, B. M. Castro, J. A. Lima, and A. D. S. Mascarenhas, 2004: On the baroclinic structure of the Brazil Current-Intermediate Western Boundary Current system at 22°–23°S. *Geophys. Res. Lett.*, 31, L14308, https://doi.org/10.1029/2004GL020036.
- —, J. A. M. Lima, A. C. K. Schmidt, W. Ceccopieri, A. Sartori, C. P. F. Franscisco, and R. F. C. Fontes, 2008: Is the meander growth in the Brazil Current system off southeast Brazil due to baroclinic instability? *Dyn. Atmos. Oceans*, 45, 187–207, https://doi.org/10.1016/j.dynatmoce.2008.01.002.
- —, F. Pereira, G. R. Flierl, I. T. Simoes-Sousa, A. Palóczy, M. Borges-Silva, and C. B. Rocha, 2023: The Brazil Current quasi-stationary unstable meanders at 22°S–23°S. *Prog. Oceanogr.*, 210, 102925, https://doi.org/10.1016/j.pocean.2022.102925.
- Dewar, W. K., and H. Meng, 1995: The propagation of submesoscale coherent vortices. *J. Phys. Oceanogr.*, **25**, 1745–1770, https://doi.org/10.1175/1520-0485(1995)025<1745:TPOSCV>2. 0.CO;2.
- Dong, J., B. Fox-Kemper, J. Zhu, and C. Dong, 2021: Application of symmetric instability parameterization in the Coastal and Regional Ocean Community Model (CROCO). J. Adv. Model. Earth Syst., 13, e2020MS002302, https://doi.org/10. 1029/2020MS002302.
- Egbert, G. D., and S. Y. Erofeeva, 2002: Efficient inverse modeling of barotropic ocean tides. *J. Atmos. Oceanic Technol.*, **19**, 183–204, https://doi.org/10.1175/1520-0426(2002)019<0183: EIMOBO>2.0.CO;2.
- Fadeev, E., and Coauthors, 2021: Submesoscale physicochemical dynamics directly shape bacterioplankton community structure in space and time. *Limnol. Oceanogr.*, 66, 2901–2913, https://doi.org/10.1002/lno.11799.
- Fernandez, E., and J. M. Lellouche, 2018: Product user manual for the global ocean physical reanalysis product GLOBAL_REANALYSIS_PHY_001_030. EU Copernicus Marine Service Rep. CMEMS-GLO-PUM-001-030, 25 pp., https://catalogue.marine.copernicus.eu/documents/PUM/CMEMS-GLO-PUM-001-030.pdf.
- Fox-Kemper, B., R. Ferrari, and R. Hallberg, 2008: Parameterization of mixed layer eddies. Part I: Theory and diagnosis. J. Phys. Oceanogr., 38, 1145–1165, https://doi.org/10.1175/2007 JPO3792.1.
- Freilich, M., and A. Mahadevan, 2021: Coherent pathways for subduction from the surface mixed layer at ocean fronts. J. Geophys. Res. Oceans, 126, e2020JC017042, https://doi.org/10. 1029/2020JC017042.
- Gula, J., M. Molemaker, and J. McWilliams, 2015: Topographic vorticity generation, submesoscale instability and vortex street formation in the Gulf Stream. *Geophys. Res. Lett.*, 42, 4054–4062, https://doi.org/10.1002/2015GL063731.
- —, M. J. Molemaker, and J. C. McWilliams, 2016a: Submesoscale dynamics of a Gulf Stream frontal eddy in the South Atlantic Bight. J. Phys. Oceanogr., 46, 305–325, https://doi. org/10.1175/JPO-D-14-0258.1.
- —, and —, 2016b: Topographic generation of submesoscale centrifugal instability and energy dissipation. *Nat. Commun.*, 7, 12811, https://doi.org/10.1038/ncomms12811.
- —, J. Taylor, A. Shcherbina, and A. Mahadevan, 2022: Submeso-scale processes and mixing. *Ocean Mixing*, Elsevier, 181–214.
- Haney, R. L., 1991: On the pressure gradient force over steep topography in sigma coordinate ocean models. J. Phys.

- Oceanogr., **21**, 610–619, https://doi.org/10.1175/1520-0485 (1991)021<0610:OTPGFO>2.0.CO;2.
- Hersbach, H., and Coauthors, 2020: The ERA5 global reanalysis. *Quart. J. Roy. Meteor. Soc.*, **146**, 1999–2049, https://doi.org/10.1002/qj.3803.
- Houry, S., E. Dombrowsky, P. De Mey, and J.-F. Minster, 1987: Brunt-Väisälä frequency and Rossby radii in the South Atlantic. *J. Phys. Oceanogr.*, **17**, 1619–1626, https://doi.org/10.1175/1520-0485(1987)017<1619:BVFARR>2.0.CO;2.
- Kang, D., and E. N. Curchitser, 2015: Energetics of eddy-mean flow interactions in the Gulf Stream region. J. Phys. Oceanogr., 45, 1103–1120, https://doi.org/10.1175/JPO-D-14-0200.1.
- Lazaneo, C. Z., D. C. Napolitano, I. C. A. da Silveira, A. Tandon, D. G. MacDonald, R. A. Ávila, and P. H. R. Calil, 2020: On the role of turbulent mixing produced by vertical shear between the Brazil Current and the intermediate western boundary current. J. Geophys. Res. Oceans, 125, e2019JC015338, https://doi.org/10.1029/2019JC015338.
- —, P. H. R. Calil, A. Tandon, and I. C. A. da Silveira, 2022: Submesoscale coherent vortices in the South Atlantic Ocean: A pathway for energy dissipation. *J. Geophys. Res. Oceans*, 127, e2020JC017099, https://doi.org/10.1029/2020JC017099.
- Lévy, M., P. J. S. Franks, and K. S. Smith, 2018: The role of sub-mesoscale currents in structuring marine ecosystems. *Nat. Commun.*, 9, 4758, https://doi.org/10.1038/s41467-018-07059-3.
- Li, J., and M. Roughan, 2023: Energetics of eddy-mean flow interactions in the East Australian current system. J. Phys. Oceanogr., 53, 595–612, https://doi.org/10.1175/JPO-D-22-0128.1.
- —, and C. Kerry, 2022: Drivers of ocean warming in the western boundary currents of the Southern Hemisphere. *Nat. Climate Change*, **12**, 901–909, https://doi.org/10.1038/s41558-022-01473-8.
- Li, Z., Y. Chao, and J. C. McWilliams, 2006: Computation of the streamfunction and velocity potential for limited and irregular domains. *Mon. Wea. Rev.*, **134**, 3384–3394, https://doi.org/ 10.1175/MWR3249.1.
- Luko, C. D., I. C. A. da Silveira, I. T. Simoes-Sousa, J. M. Araujo, and A. Tandon, 2021: Revisiting the Atlantic South Equatorial Current. J. Geophys. Res. Oceans, 126, e2021JC017387, https://doi.org/10.1029/2021JC017387.
- Magalhães, F. C., J. L. L. Azevedo, and L. R. Oliveira, 2017: Energetics of eddy-mean flow interactions in the Brazil current between 20°S and 36°S. J. Geophys. Res. Oceans, 122, 6129–6146, https://doi.org/10.1002/2016JC012609.
- Mahadevan, A., 2016: The impact of submesoscale physics on primary productivity of plankton. *Annu. Rev. Mar. Sci.*, 8, 161–184, https://doi.org/10.1146/annurev-marine-010814-015912.
- McWilliams, J. C., 2016: Submesoscale currents in the ocean. Proc. Roy. Soc., 472A, 20160117, https://doi.org/10.1098/rspa. 2016.0117.
- —, J. Gula, and M. J. Molemaker, 2019: The Gulf Stream North Wall: Ageostrophic circulation and frontogenesis. J. Phys. Oceanogr., 49, 893–916, https://doi.org/10.1175/JPO-D-18-0203.1.
- Mill, G. N., V. S. da Costa, N. D. Lima, M. Gabioux, L. A. A. Guerra, and A. M. Paiva, 2015: Northward migration of Cape São Tomé rings, Brazil. Cont. Shelf Res., 106, 27–37, https://doi.org/10.1016/j.csr.2015.06.010.
- Molemaker, M. J., J. C. McWilliams, and W. K. Dewar, 2015: Submesoscale instability and generation of mesoscale anticyclones near a separation of the California undercurrent. *J. Phys. Oceanogr.*, 45, 613–629, https://doi.org/10.1175/JPO-D-13-0225.1.

- Morvan, M., P. L'Hégaret, X. Carton, J. Gula, C. Vic, C. de Marez, M. Sokolovskiy, and K. Koshel, 2019: The life cycle of submesoscale eddies generated by topographic interactions. *Ocean Sci.*, 15, 1531–1543, https://doi.org/10.5194/os-15-1531-2019.
- Müller, P., J. C. McWilliams, and M. J. Molemaker, 2005: Routes to dissipation in the ocean: The 2D/3D turbulence conundrum. *Marine Turbulence: Theories, Observations and Models*, H. Baumert, J. Simpson, and J. Sundermann, Eds., Cambridge University Press, 397–405.
- Napolitano, D. C., I. C. A. da Silveira, C. B. Rocha, G. R. Flierl, P. H. R. Calil, and R. P. Martins, 2019: On the steadiness and instability of the intermediate western boundary current between 24° and 18°S. *J. Phys. Oceanogr.*, **49**, 3127–3143, https://doi.org/10.1175/JPO-D-19-0011.1.
- —, C. B. Rocha, I. C. A. da Silveira, I. T. Simoes-Sousa, and G. R. Flierl, 2021a: Can the intermediate Western Boundary Current recirculation trigger the Vitória eddy formation? *Ocean Dyn.*, 71, 281–292, https://doi.org/10.1007/s10236-020-01437-6.
- —, I. C. A. da Silveira, A. Tandon, and P. H. R. Calil, 2021b: Submesoscale phenomena due to the Brazil Current crossing of the Vitória-Trindade Ridge. *J. Geophys. Res. Oceans*, 126, e2020JC016731, https://doi.org/10.1029/2020JC016731.
- Palóczy, A., I. C. A. da Silveira, B. M. Castro, and L. Calado, 2014: Coastal upwelling off Cape São Tomé (22°S, Brazil): The supporting role of deep ocean processes. *Cont. Shelf Res.*, 89, 38–50, https://doi.org/10.1016/j.csr.2013.09.005.
- Pereira, F., I. C. A. da Silveira, G. R. Flierl, and A. Tandon, 2019: NPZ response to eddy-induced upwelling in a Brazil Current ring: A theoretical approach. *Dyn. Atmos. Oceans*, 87, 101096, https://doi.org/10.1016/j.dynatmoce.2019.101096.
- Rocha, C. B., and I. T. Simoes-Sousa, 2022: Compact mesoscale eddies in the South Brazil Bight. *Remote Sens.*, 14, 5781, https://doi.org/10.3390/rs14225781.
- —, I. C. A. da Silveira, B. M. Castro, and J. A. M. Lima, 2014: Vertical structure, energetics, and dynamics of the Brazil Current System at 22°S–28°S. *J. Geophys. Res. Oceans*, **119**, 52–69, https://doi.org/10.1002/2013JC009143.
- Rodrigues, R. R., L. M. Rothstein, and M. Wimbush, 2007: Seasonal variability of the South Equatorial Current bifurcation in the Atlantic Ocean: A numerical study. *J. Phys. Oceanogr.*, 37, 16–30, https://doi.org/10.1175/JPO2983.1.
- Schmid, C., and S. Majumder, 2018: Transport variability of the Brazil Current from observations and a data assimilation model. *Ocean Sci.*, 14, 417–436, https://doi.org/10.5194/os-14-417-2018.
- Schubert, R., and W. Rath, 2021: reneschubert/keflux: Computing the oceanic kinetic energy flux across spatial scales using coarse-graining (version v.1.0.1). Zenodo, accessed 1 February 2021, https://doi.org/10.5281/zenodo.4486265.
- —, J. Gula, R. J. Greatbatch, B. Baschek, and A. Biastoch, 2020: The submesoscale kinetic energy cascade: Mesoscale absorption of submesoscale mixed layer eddies and frontal downscale fluxes. J. Phys. Oceanogr., 50, 2573–2589, https:// doi.org/10.1175/JPO-D-19-0311.1.
- —, and A. Biastoch, 2021: Submesoscale flows impact Agulhas leakage in ocean simulations. *Commun. Earth Environ.*, **2**, 197, https://doi.org/10.1038/s43247-021-00271-y.
- Shchepetkin, A. F., and J. C. McWilliams, 2005: The Regional Oceanic Modeling System (ROMS): A split-explicit, free-surface, topography-following-coordinate oceanic model.

- Ocean Modell., 9, 347–404, https://doi.org/10.1016/j.ocemod. 2004.08.002.
- Shcherbina, A. Y., E. A. D'Asaro, C. M. Lee, J. M. Klymak, M. J. Molemaker, and J. C. McWilliams, 2013: Statistics of vertical vorticity, divergence, and strain in a developed submesoscale turbulence field. *Geophys. Res. Lett.*, 40, 4706–4711, https://doi.org/10.1002/grl.50919.
- Soufflet, Y., P. Marchesiello, F. Lemarié, J. Jouanno, X. Capet, L. Debreu, and R. Benshila, 2016: On effective resolution in ocean models. *Ocean Modell.*, 98, 36–50, https://doi.org/10.1016/j.ocemod.2015.12.004.
- Soutelino, R. G., I. C. A. da Silveira, A. Gangopadhyay, and J. A. Miranda, 2011: Is the Brazil current eddy-dominated to the North of 20°S? *Geophys. Res. Lett.*, 38, L03607, https://doi.org/10.1029/2010GL046276.
- Srinivasan, K., J. C. McWilliams, M. J. Molemaker, and R. Bar-kan, 2019: Submesoscale vortical wakes in the lee of topography. *J. Phys. Oceanogr.*, 49, 1949–1971, https://doi.org/10.1175/JPO-D-18-0042.1.
- Stramma, L., and M. England, 1999: On the water masses and mean circulation of the South Atlantic Ocean. J. Geophys. Res., 104, 20863–20883, https://doi.org/10.1029/1999JC900139.
- Taylor, J. R., and A. F. Thompson, 2023: Submesoscale dynamics in the upper ocean. *Annu. Rev. Fluid Mech.*, 55, 103–127, https://doi.org/10.1146/annurev-fluid-031422-095147.
- Theisel, H., and U. Rauschenbach, 1999: Curvis-visualizing the curvature of vector fields on the internet. *Rostocker Inf.-Ber.*, **23**, 105–114.
- Thomas, L. N., A. Tandon, and A. Mahadevan, 2008: Submeso-scale processes and dynamics. *Ocean Modeling in an Eddying Regime*, *Geophys. Monogr.*, Vol. 177, Amer. Geophys. Union, 17–38, https://doi.org/10.1029/177GM04.
- —, J. R. Taylor, R. Ferrari, and T. M. Joyce, 2013: Symmetric instability in the Gulf Stream. *Deep-Sea Res. II*, **91**, 96–110, https://doi.org/10.1016/j.dsr2.2013.02.025.
- —, —, E. A. D'Asaro, C. M. Lee, J. M. Klymak, and A. Shcherbina, 2016: Symmetric instability, inertial oscillations, and turbulence at the Gulf Stream front. *J. Phys. Oceanogr.*, **46**, 197–217, https://doi.org/10.1175/JPO-D-15-0008.1.
- Uchoa, I., I. T. Simoes-Sousa, and I. C. A. da Silveira, 2023: The Brazil Current mesoscale eddies: Altimetry-based characterization and tracking. *Deep-Sea Res. I*, 192, 103947, https://doi. org/10.1016/j.dsr.2022.103947.
- Vic, C., G. Roullet, X. Capet, X. Carton, M. J. Molemaker, and J. Gula, 2015: Eddy-topography interactions and the fate of the Persian Gulf Outflow. J. Geophys. Res. Oceans, 120, 6700–6717, https://doi.org/10.1002/2015JC011033.
- Wenegrat, J. O., and L. N. Thomas, 2020: Centrifugal and symmetric instability during Ekman adjustment of the bottom boundary layer. *J. Phys. Oceanogr.*, 50, 1793–1812, https://doi.org/10.1175/JPO-D-20-0027.1.
- —, J. Callies, and L. N. Thomas, 2018: Submesoscale baroclinic instability in the bottom boundary layer. *J. Phys. Oceanogr.*, 48, 2571–2592, https://doi.org/10.1175/JPO-D-17-0264.1.
- Yan, X., D. Kang, E. N. Curchitser, and C. Pang, 2019: Energetics of eddy-mean flow interactions along the western boundary currents in the North Pacific. J. Phys. Oceanogr., 49, 789–810, https://doi.org/10.1175/JPO-D-18-0201.1.
- —, —, C. Pang, L. Zhang, and H. Liu, 2022: Energetics analysis of the eddy–Kuroshio interaction east of Taiwan. *J. Phys. Oceanogr.*, **52**, 647–664, https://doi.org/10.1175/JPO-D-21-0198.1.